The HKU Scholars Hub   The University of Hong Kong   香港大學學術庫

Title	**Stabilized Plane and Axisymmetric Lobatto Finite Element Models**
Author(s)	**Hu, YC; Sze, KY; Zhou, YX**
Citation	**Computational Mechanics, 2015, v. 56 n. 5, p. 879-903**
Issued Date	**2015**
URL	**http://hdl.handle.net/10722/221459**
Rights	**The final publication is available at Springer via http://dx.doi.org/10.1007/s00466-015-1207-5; This work is licensed under a Creative Commons Attribution-NonCommercial-NoDerivatives 4.0 International License.**

Stabilized Plane and Axisymmetric Lobatto Finite Element Models

Y.C.Hu, K.Y.Sze[*], Y.X.Zhou

Department of Mechanical Engineering, The University of Hong Kong, Pokfulam, Hong Kong.
* Correspondence author (Email: kysze@hku.hk)

ABSTRACT

High order elements are renowned for their high accuracy and convergence. Among them, Lobatto spectral finite elements are commonly used in explicit dynamic analyses as their mass matrices when evaluated by the Lobatto integration rule are diagonal. While there are numerous advanced first and second order elements, advanced high order elements are rarely seen. In this paper, generic stabilization schemes are devised for the reduced integrated plane and axisymmetric elements. Static and explicit dynamic tests are considered for evaluating the relatively merits of the stabilized and conventional elements. The displacement errors of the stabilized elements are less than those of the conventional Lobatto elements. When the material is nearly incompressible, the stabilized elements are also more accurate in terms of the energy error norm. This advantage is of practical importance for bio-tissue and hydrated soil analyses.

Keywords: spectral finite element, Lagrange element, stabilization, hybrid, Lobatto element

1. INTRODUCTION

Given that $L_i(\xi)$ is the 1D interpolant of node-i at ξ_i, the interpolation function of the node-(i,j) at (ξ_i, η_j) of the 2D Lagrange element is the tensor product $L_i(\xi)L_j(\eta)$ in which (ξ, η) are the natural coordinates. Interpolants for Lagrange elements with equispaced nodes suffer from the Runge phenomenon in which, as the number of nodes increases, the functions exhibit undesirable level of oscillation near the boundary of the interpolation range. To overcome the oscillation, Chebyshev and Lobatto (also known as Lobatto-Legendre) nodes have been used in the context of the spectrum finite elements [1-10]. Among them, Lobatto elements using the Lobatto nodes are often integrated by the Lobatto (also known as Gauss-Lobatto) rule in which the integration points are the Lobatto nodes. Thus, the element mass matrices are diagonal and can readily be used in the explicit time integration. Moreover, the derivatives of the Lagrange interpolant at node-(i,j) depend only on the nodes along $\xi = \xi_i$ and $\eta = \eta_j$. They can be efficiently computed using the coefficient matrices of the spectrum method. Note worthily, Lobatto elements have recently been advocated as the differential quadrature elements [11, 12].

The first and second order Lagrange plane elements are also known as bilinear and biquadratic elements, respectively. They have been the subjects of research for several decades. In this light, advanced formulations including but not limited to hybrid/mixed formulation [13-20], SRI (selectively reduced integration) [21, 22], stabilization [14-18, 23-29], incompatible displacement or EAS (enhanced assumed strain) method [30-34] have been proposed. However, advanced high order elements are rarely seen, probably because they are seldom used in stress analysis and advanced formulations also become more expensive in high order elements. For example, a large number of assumed stress/strain and EAS modes would be expected in high order elements. On the other hand, high order Lobatto elements are commonly employed in analyzing wave dynamics including geophysics simulations due to their low numerical dispersion and their advantage in explicit time integration [3, 4, 7-9].

Among the advanced formulations, stabilization employs a small number of stabilization vectors. These vectors are orthogonal to the element displacement vectors arising from rigid body and constant strain modes whilst their matrix products can stabilize the URI (uniformly reduced integrated) element. The earliest stabilizations derive the stabilization vectors by decomposing the element displacement into rigid body, constant strain and the hourglass modes. If necessary, Gram Schmidt orthogonalization has to be used for required orthogonality [23, 24]. On the other hand, Lee & Rhiu [14, 15] use a hybrid strain approach to formulate the stabilization vectors. Low and high order hybrid strain modes are assumed. The low order strain leads to the URI element. The stabilization vectors are present in the difference of the two leverage matrices associated with the

high order hybrid strain modes. The integrands leading to the two leverage matrices are identical but are integrated by different quadrature rules. Sze employs a hybrid stress approach with low and high order hybrid stress modes [16-18]. Similar to Lee & Rhiu's approach, the low order hybrid stress modes lead to the URI element. However, the low and high order hybrid stress modes are somehow orthogonal in the flexibility matrix and the stabilization vectors are the row vectors of the leverage matrix [16] which can be derived explicitly. It is worth mentioning that predictions of EAS elements in large deformation may also be plagued by hourglass modes when the elements are under finite compressive strain. The earlier remedy is to modify the displacement gradient of some EAS modes [31, 32]. More recently, a stabilization method was devised by Reese & Wriggers [26]. The method can automatically invoke the stabilization stiffness in the tangential stiffness matrix.

We have noted that all plane URI Lagrange elements with order two or above possess only two compatible and one incompatible spurious zero energy modes. Hence, stabilization appears to be an efficient choice for advanced high order elements and will be devised for plane and axisymmetric Lobatto elements of any order by generalizing the hybrid stress approach of Sze and his coworkers modes [16-18]. The stabilized elements are less stiff than the standard elements in general. While they are also more accurate than the standard elements for nearly incompressible material analysis, they suffer the pressure oscillation in the stringent driven cavity problem. The oscillation, however, can be eliminated by a simple method which reduces the rank of the penalty matrix.

Throughout this paper, 1D and 2D arrays are underlined and double-underlined, respectively.

2. STANDARD LOBATTO ELEMENT

In this section, the 2D n-th order Lobatto element is introduced. The set of 1D Lobatto nodes $\{l_i, i = 1, .., n, n+1\}$ are the roots in increasing order of

$$(1-\xi^2)P_n'(\xi) = 0 \tag{1}$$

in which P_n denotes the degree-n Legendre polynomial. The smallest and largest roots are always at -1 and +1 which define the element boundary [6, 35] and the Lobatto nodes cluster around $\xi = \pm 1$, see Figure 1. For 2D Lobatto element with natural coordinates (ξ, η), node-(i,j) is at (l_i, l_j), see Figure 2(a). In Lagrange elements, the interpolants can be obtained by tensor product. Thus, the interpolated global coordinates and displacements are:

$$\underline{x} = \begin{Bmatrix} x \\ y \end{Bmatrix} = \sum_{i,j=1}^{n+1} L_i(\xi)L_j(\eta) \begin{Bmatrix} x_{ij} \\ y_{ij} \end{Bmatrix} , \quad \underline{u} = \begin{Bmatrix} u \\ v \end{Bmatrix} = \sum_{i,j=1}^{n+1} L_i(\xi)L_j(\eta) \begin{Bmatrix} u_{ij} \\ v_{ij} \end{Bmatrix} = \underline{\underline{N}}\,\underline{d} \tag{2}$$

where

$$L_i(\xi) = \frac{(\xi - l_1)\cdots(\xi - l_{i-1})(\xi - l_{i+1})\cdots(\xi - l_n)(\xi - l_{n+1})}{(l_i - l_1)\cdots(l_i - l_{i-1})(l_i - l_{i+1})\cdots(l_i - l_n)(l_i - l_{n+1})}$$ is the 1D Lagrangian interpolation,

x_{ij} and y_{ij} are the nodal Cartesian coordinates,

u_{ij} and v_{ij} are the nodal displacements,

$\underline{N}$ is the displacement interpolation matrix,

$\underline{d}$ is the element displacement vector that contains all u_{ij}s and v_{ij}s.
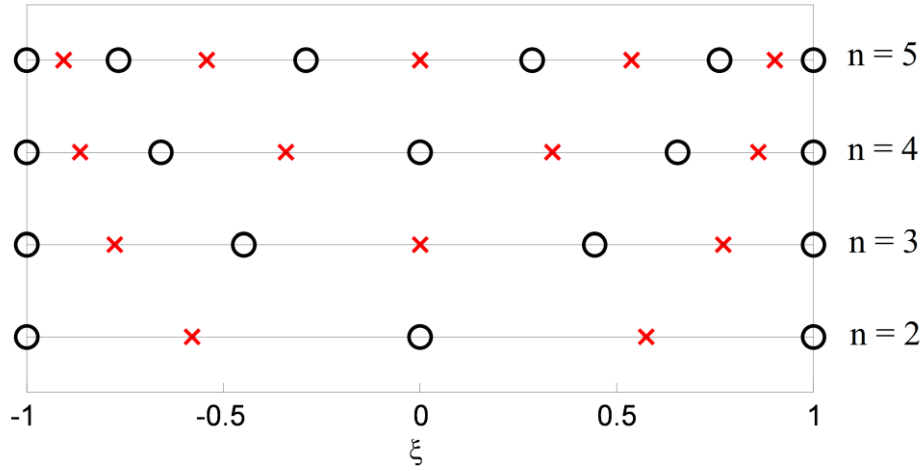

Figure 1. The $(n+1)$-point Lobatto nodes $\bigcirc$ and n-point Gaussian quadrature points $\times$ along ξ.
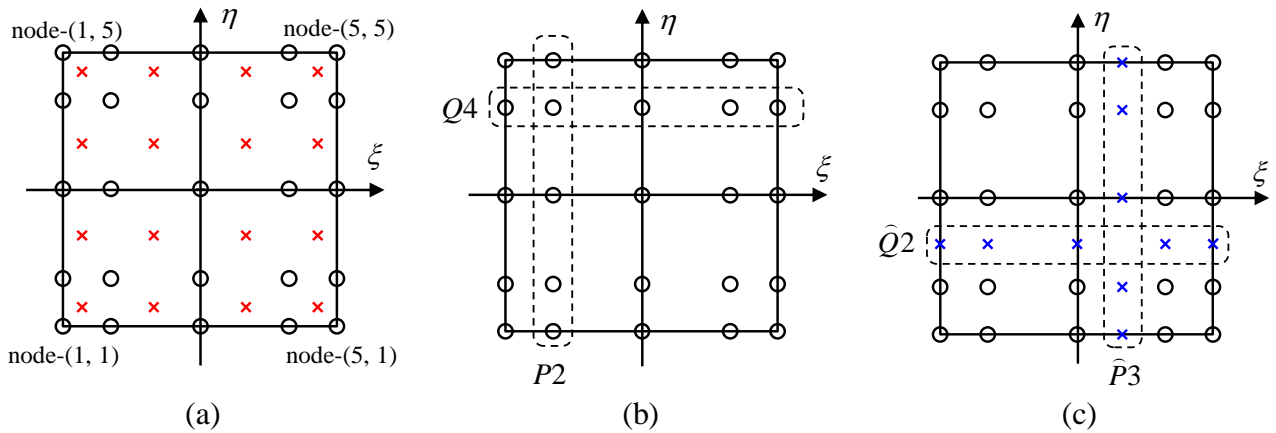

Figure 2. (a) The 5×5 Lobatto nodes $\bigcirc$ and the 4×4 Gaussian points $\times$, (b) nodes $\bigcirc$ in node sets $P2$ and $Q4$, (c) auxiliary nodes $\times$ in auxiliary node sets $\hat{P}3$ and $\hat{Q}2$.

By invoking the interpolations in (2), the strain-displacement relation can be expressed as:

$$\underline{\varepsilon} = \begin{Bmatrix} \varepsilon_x \\ \varepsilon_y \\ \gamma_{xy} \end{Bmatrix} = \begin{Bmatrix} u_{,x} \\ v_{,y} \\ u_{,y} + v_{,x} \end{Bmatrix} = \underline{\underline{B}}\,\underline{d} \tag{3}$$

in which $\underline{\underline{B}}$ is the strain-displacement matrix. The following gives the total potential for the element "e":

$$\Pi_P^e = \frac{1}{2}\langle \underline{\varepsilon}^T \underline{\underline{C}}\, \underline{\varepsilon}\rangle^e - P^e \qquad (4)$$

in which $\underline{\underline{C}}$ is the material stiffness matrix and P^e is the work done by the external loads and the element domain integral operator is

$$\langle \circ \rangle^e = \int\limits_{-1}^{+1}\int\limits_{-1}^{+1} \circ J d\xi d\eta \qquad (5)$$

where $J = \dfrac{\partial x}{\partial \xi}\dfrac{\partial y}{\partial \eta} - \dfrac{\partial x}{\partial \eta}\dfrac{\partial y}{\partial \xi}$ is the Jacobian determinant. Substituting (3) into (4) yields,

$$\Pi_P^e = \frac{1}{2}\underline{d}^T \langle \underline{\underline{B}}^T \underline{\underline{C}}\,\underline{\underline{B}}\rangle^e \underline{d} - P^e = \frac{1}{2}\underline{d}^T \underline{\underline{k}}\,\underline{d} - P^e \qquad (6)$$

where $\underline{\underline{k}} = \langle \underline{\underline{B}}^T \underline{\underline{C}}\,\underline{\underline{B}}\rangle^e$ is the element stiffness matrix. The stiffness matrix of the conventional Lobatto element is:

$$\underline{\underline{k}}_{LB} = \langle \underline{\underline{B}}^T \underline{\underline{C}}\,\underline{\underline{B}}\rangle_{LBQ} \qquad (7)$$

In the expression, $\langle\rangle_{LBQ}$ denotes that the integration $\langle\rangle^e$ is conducted by the Lobatto quadrature (LBQ) which uses Lobatto nodes as sampling points. Note worthily, the strain at a node depends on a small subset of element nodes. Hence, the element stiffness can be more efficiently formed by an assembling procedure, see Appendix.

3. URI LOBATTO ELEMENT AND ITS ZERO ENERGY MODES

The stiffness matrix of the URI (uniformly reduced integration) Lobatto element can be expressed as:

$$\underline{\underline{k}}_{URI} = \langle \underline{\underline{B}}^T \underline{\underline{C}}\,\underline{\underline{B}}\rangle_{RGQ} = \sum_{i=1}^{n}\sum_{j=1}^{n} \widehat{w}_i \widehat{w}_j \widehat{J}_{ij}\, \underline{\underline{\widehat{B}}}_{ij}^T \underline{\underline{C}}\,\underline{\underline{\widehat{B}}}_{ij} . \qquad (8)$$

where $\langle\rangle_{RGQ}$ denotes that the integration $\langle\rangle^e$ is conducted by the low order or reduced order Gaussian quadrature (RGQ) with sampling stations $(g_1,\ldots,g_n)$ and the weight factors $(\widehat{w}_1,\ldots,\widehat{w}_n)$. Moreover, the capped and indexed Jacobian determinant and the B-matrix are defined as:

$$\widehat{J}_{ij} = J\Big|_{(\xi=g_i,\eta=g_j)} \ , \ \underline{\underline{\widehat{B}}}_{ij} = \underline{\underline{B}}\Big|_{(\xi=g_i,\eta=g_j)}. \qquad (9)$$

For the bilinear and biquadratic URI elements, the zero energy modes are well-documented [14, 16, 24]. For the bi-unit square element geometry, they can be expressed as:

$$\begin{Bmatrix} u_\xi \\ u_\eta \end{Bmatrix} = \begin{Bmatrix} \xi\eta \\ 0 \end{Bmatrix}, \begin{Bmatrix} 0 \\ \xi\eta \end{Bmatrix} \quad \text{and} \quad \begin{Bmatrix} u_\xi \\ u_\eta \end{Bmatrix} = \begin{Bmatrix} (\xi^2 - \frac{1}{3})(\eta^2 - \frac{1}{3}) \\ 0 \end{Bmatrix}, \begin{Bmatrix} 0 \\ (\xi^2 - \frac{1}{3})(\eta^2 - \frac{1}{3}) \end{Bmatrix}, \begin{Bmatrix} \xi(\eta^2 - \frac{1}{3}) \\ -\eta(\xi^2 - \frac{1}{3}) \end{Bmatrix}.$$

From our derivation, the number of zero energy modes remains to be three for element order $n \geq 2$ and the modes are

$$\begin{Bmatrix} u_\xi \\ u_\eta \end{Bmatrix} = \begin{Bmatrix} P_n(\xi)P_n(\eta) \\ 0 \end{Bmatrix}, \begin{Bmatrix} 0 \\ P_n(\xi)P_n(\eta) \end{Bmatrix}, \begin{Bmatrix} P'_n(\xi)P_n(\eta) \\ -P_n(\xi)P'_n(\eta) \end{Bmatrix} \tag{10}$$

Since the n-point Gaussian quadrature points are the roots of P_n, it is trivial that strains arising from the above modes vanish at all the sampling points of the RGQ. Among them, the last one is incompatible, i.e. it is self-inhibited in a mesh with more than one element.

To verify the incompatibility of the last mode, two un-deformed bi-unit square elements "a" and "b" shown in Figure 3 are considered. For even n, P_n and P'_n are even and odd functions, respectively. In order that both elements have the same u_ξ along their common edge where $\xi = 1$ for "a" and $\xi = -1$ for "b", the third mode is

$$\begin{Bmatrix} u_\xi^a \\ u_\eta^a \end{Bmatrix} = \begin{Bmatrix} P'_n(1)P_n(\eta) \\ -P_n(1)P'_n(\eta) \end{Bmatrix} \quad \text{and} \quad \begin{Bmatrix} u_\xi^b \\ u_\eta^b \end{Bmatrix} = -\begin{Bmatrix} P'_n(-1)P_n(\eta) \\ -P_n(-1)P'_n(\eta) \end{Bmatrix} = \begin{Bmatrix} P'_n(1)P_n(\eta) \\ P_n(1)P'_n(\eta) \end{Bmatrix}.$$

The disagreement in u_η implies incompatibility. For other n and orientations of the natural coordinates (ξ, η), the incompatibility can be similarly verified.
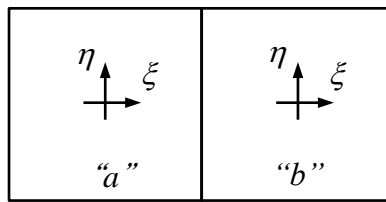

Figure 3. Two bi-unit square elements "a" and "b" for the incompatibility check of the third mode.

4. STABILIZATION USING A HYBRID STRESS FUNCTIONAL

The stabilization method to be introduced employs Hellinger-Reissner functional. Its elementwise version can be expressed as:

$$\Pi_{HR}^e = \langle -\frac{1}{2}\underline{\sigma}^T \underline{\underline{C}}^{-1} \underline{\sigma} + \underline{\sigma}^T \underline{\varepsilon} \rangle^e - P^e \tag{11}$$

in which $\underline{\sigma}$ is the vector of assumed stress components. To formulate the stabilization scheme, the assumed $\underline{\sigma}$ is first expressed as modes [16-18]:

$$\underline{\sigma} = \underline{\sigma}_L + \underline{\sigma}_H \tag{12}$$

where the subscripts "L" and "H" denote low and high order modes, respectively. If they are chosen to be orthogonal, i.e.

$$\langle \underline{\sigma}_L^T \underline{\underline{C}}^{-1} \underline{\sigma}_H \rangle^e = 0, \tag{13}$$

the functional becomes:

$$\Pi_{HR}^e = \langle -\frac{1}{2} \underline{\sigma}_L^T \underline{\underline{C}}^{-1} \underline{\sigma}_L + \underline{\sigma}_L^T \underline{\varepsilon} \rangle^e + \langle -\frac{1}{2} \underline{\sigma}_H^T \underline{\underline{C}}^{-1} \underline{\sigma}_H + \underline{\sigma}_H^T \underline{\varepsilon} \rangle^e - P^e \tag{14}$$

The core idea of stabilizing the URI element using the hybrid-stress formulation is that the low order stress modes would lead to the uniformly reduced integrated element and the high order stress modes play the role of stabilizing the URI element [16-18].

4.1 LOW ORDER STRESS MODES AND URI ELEMENT

Low order stress modes which can lead to the URI bilinear and biquadratic elements can be found in [16-18, 21]. For the high order element, the following set of low order stress modes is considered:

$$\underline{\sigma}_L = \begin{Bmatrix} \sigma_x \\ \sigma_y \\ \sigma_{xy} \end{Bmatrix}_L = \sum_{i,j=1}^{n} G_i(\xi) G_j(\eta) \begin{Bmatrix} \alpha_{ij}^x \\ \alpha_{ij}^y \\ \alpha_{ij}^{xy} \end{Bmatrix} = \sum_{i,j=1}^{n} G_i(\xi) G_j(\eta) \underline{\alpha}_{ij} \tag{15}$$

where $\underline{\alpha}_{ij}$ is the vector of coefficients and G_i is the 1D Lagrange interpolating polynomial for the RGQ station g_i, i.e.

$$G_i(\xi) = \frac{(\xi - g_1) \cdots (\xi - g_{i-1})(\xi - g_{i+1}) \cdots (\xi - g_n)}{(g_i - g_1) \cdots (g_i - g_{i-1})(g_i - g_{i+1}) \cdots (g_i - g_n)} \quad \text{and} \quad G_i(g_j) = \delta_{ij} \tag{16}$$

As G_i is a degree n-1 polynomial, the first integral in (14) is of degrees $2n$-1 in ξ and η for regular elements and can be evaluated by RGQ using which the integral becomes

$$\langle -\frac{1}{2} \underline{\sigma}_L^T \underline{\underline{C}}^{-1} \underline{\sigma}_L + \underline{\sigma}_L^T \underline{\varepsilon} \rangle_{RGQ} = \sum_{i=1}^{n} \sum_{j=1}^{n} \widehat{w}_i \widehat{w}_j \widehat{J}_{ij} (-\frac{1}{2} \underline{\alpha}_{ij}^T \underline{\underline{C}}^{-1} \underline{\alpha}_{ij} + \underline{\alpha}_{ij}^T \underline{\widehat{B}}_{ij} \underline{d}) \tag{17}$$

The zero variation of (14) or (17) with respect to $\underline{\alpha}_{ij}$ yields

$$\underline{\alpha}_{ij} = \underline{\underline{C}} \underline{\widehat{B}}_{ij} \underline{d} \quad \text{and} \quad \underline{\sigma}_L = \begin{Bmatrix} \sigma_x \\ \sigma_y \\ \sigma_{xy} \end{Bmatrix}_L = \sum_{i,j=1}^{n} G_i(\xi) G_j(\eta) \underline{\underline{C}} \underline{\widehat{B}}_{ij} \underline{d} \tag{18}$$

and (17) becomes

$$\langle -\frac{1}{2}\underline{\sigma}_L^T \underline{\underline{C}}^{-1}\underline{\sigma}_L + \underline{\sigma}_L^T \underline{\varepsilon}\rangle_{RGQ} = \frac{1}{2}\underline{d}^T \sum_{i=1}^{n}\sum_{j=1}^{n}\hat{w}_i\hat{w}_j\hat{J}_{ij}\underline{\hat{B}}_{ij}^T\underline{\underline{C}}\underline{\hat{B}}_{ij}\underline{d} = \frac{1}{2}\underline{d}^T\underline{\underline{k}}_{URI}\underline{d} \tag{19}$$

where $\underline{k}_{URI}$ is the URI element stiffness matrix in (8).

4.2 HIGH ORDER STRESS MODES

Further to the discussion on the zero energy modes in (10), the covariant strain derived from the zero energy modes are

$$\begin{Bmatrix}\varepsilon_{\xi\xi}\\ \varepsilon_{\eta\eta}\\ 2\varepsilon_{\xi\eta}\end{Bmatrix} = \begin{bmatrix}\partial/\partial\xi & 0\\ 0 & \partial/\partial\eta\\ \partial/\partial\eta & \partial/\partial\xi\end{bmatrix}\begin{bmatrix}P_n(\xi)P_n(\eta) & 0 & P_n'(\xi)P_n(\eta)\\ 0 & P_n(\xi)P_n(\eta) & -P_n(\xi)P_n'(\eta)\end{bmatrix}\begin{Bmatrix}c_1\\ c_2\\ c_3\end{Bmatrix}$$

$$= \begin{bmatrix}P_n'(\xi)P_n(\eta) & 0 & P_n''(\xi)P_n(\eta)\\ 0 & P_n(\xi)P_n'(\eta) & -P_n(\xi)P_n''(\eta)\\ P_n(\xi)P_n'(\eta) & P_n'(\xi)P_n(\eta) & 0\end{bmatrix}\begin{Bmatrix}c_1\\ c_2\\ c_3\end{Bmatrix} \tag{20}$$

where c's are coefficients. The following contravariant stress modes are chosen to stabilize the zero energy modes:

$$\begin{Bmatrix}\sigma_{\xi\xi}\\ \sigma_{\eta\eta}\\ \sigma_{\xi\eta}\end{Bmatrix} = \frac{1}{J}\begin{bmatrix}P_n'(\xi)P_n(\eta) & 0 & P_n''(\xi)P_n(\eta)\\ 0 & P_n(\xi)P_n'(\eta) & -P_n(\xi)P_n''(\eta)\\ 0 & 0 & 0\end{bmatrix}\underline{\beta} = \frac{1}{J}\underline{\underline{P}}\underline{\beta} \tag{21}$$

and its physical counterpart can be obtained as:

$$\underline{\sigma}_H = \begin{bmatrix}x,_\xi x,_\xi & x,_\eta x,_\eta & 2x,_\xi x,_\eta\\ y,_\xi y,_\xi & y,_\eta y,_\eta & 2y,_\xi y,_\eta\\ x,_\xi y,_\xi & x,_\eta y,_\eta & x,_\xi y,_\eta + y,_\xi x,_\eta\end{bmatrix}\begin{Bmatrix}\sigma_{\xi\xi}\\ \sigma_{\eta\eta}\\ \sigma_{\xi\eta}\end{Bmatrix} = \frac{1}{J}\underline{\underline{T}}\underline{\underline{P}}\underline{\beta} \tag{22}$$

In the last two equations, $\underline{P}$ and $\underline{T}$ are self-defined. On the other hand, the displacement-derived physical strain can be expressed as:

$$\underline{\varepsilon} = \begin{Bmatrix}\varepsilon_{xx}\\ \varepsilon_{yy}\\ 2\varepsilon_{xy}\end{Bmatrix} = \underline{\underline{T}}^{-T}\begin{Bmatrix}\varepsilon_{\xi\xi}\\ \varepsilon_{\eta\eta}\\ 2\varepsilon_{\xi\eta}\end{Bmatrix} = \underline{\underline{T}}^{-T}\begin{Bmatrix}\underline{x},_\xi^T \underline{u},_\xi\\ \underline{x},_\eta^T \underline{u},_\eta\\ \underline{x},_\xi^T \underline{u},_\eta + \underline{x},_\eta^T \underline{u},_\xi\end{Bmatrix} \tag{23}$$

From (2), (22) and (23), the second integral in (14) becomes

$$\langle -\frac{1}{2}\underline{\sigma}_H^T \underline{\underline{C}}^{-1}\underline{\sigma}_H + \underline{\sigma}_H^T \underline{\varepsilon}\rangle^e = -\frac{1}{2}\underline{\beta}^T\underline{\underline{H}}\underline{\beta} + \underline{\beta}^T\underline{\underline{G}}\underline{d} \tag{24}$$

where

$$\underline{\underline{H}} = \langle \frac{1}{J^2} \underline{\underline{P}}^T \underline{\underline{T}}^T \underline{\underline{C}}^{-1} \underline{\underline{T}} \underline{\underline{P}} \rangle^e = \int\limits_{-1}^{+1}\int\limits_{-1}^{+1} \frac{1}{J} \underline{\underline{P}}^T \underline{\underline{S}} \underline{\underline{P}} d\xi d\eta ,$$

$$\underline{\underline{G}}\underline{d} = \begin{bmatrix} \underline{G}_1^T \\ \underline{G}_2^T \\ \underline{G}_3^T \end{bmatrix} \underline{d} = \left\langle \frac{1}{J} \underline{\underline{P}}^T \begin{Bmatrix} \underline{x}_{,\xi}^T \underline{u}_{,\xi} \\ \underline{x}_{,\eta}^T \underline{u}_{,\eta} \\ \underline{x}_{,\xi}^T \underline{u}_{,\eta} + \underline{x}_{,\eta}^T \underline{u}_{,\xi} \end{Bmatrix} \right\rangle^e = \int\limits_{-1}^{+1}\int\limits_{-1}^{+1} \begin{Bmatrix} P_n'(\xi)P_n(\eta)\underline{x}_{,\xi}^T \underline{u}_{,\xi} \\ P_n(\xi)P_n'(\eta)\underline{x}_{,\eta}^T \underline{u}_{,\eta} \\ P_n''(\xi)P_n(\eta)\underline{x}_{,\xi}^T \underline{u}_{,\xi} - P_n(\xi)P_n''(\eta)\underline{x}_{,\eta}^T \underline{u}_{,\eta} \end{Bmatrix} d\xi d\eta$$

In the expression for $\underline{\underline{H}}$, $\underline{\underline{\tilde{S}}} = \underline{\underline{T}}^T \underline{\underline{C}}^{-1} \underline{\underline{T}}$. Substituting (2) into $\underline{\underline{G}}$,

$$\underline{G}_1^T \underline{d} = \sum_{i,j,k,l=1}^{n+1} \int\limits_{-1}^{+1}\int\limits_{-1}^{+1} P_n'(\xi)P_n(\eta)L_i'(\xi)L_j(\eta)L_k'(\xi)L_l(\eta)d\xi d\eta \cdot \underline{x}_{ij}^T \underline{u}_{kl} = \sum_{i,j,k,l=1}^{n+1} A_{ik}^1 A_{jl}^0 \cdot \underline{x}_{ij}^T \underline{u}_{kl} ,$$

$$\underline{G}_2^T \underline{d} = \sum_{i,j,k,l=1}^{n+1} \int\limits_{-1}^{+1}\int\limits_{-1}^{+1} P_n(\xi)P_n'(\eta)L_i(\xi)L_j'(\eta)L_k(\xi)L_l'(\eta)d\xi d\eta \cdot \underline{x}_{ij}^T \underline{u}_{kl} = \sum_{i,j,k,l=1}^{n+1} A_{ik}^1 A_{jl}^0 \cdot \underline{x}_{ij}^T \underline{u}_{kl} ,$$

$$\underline{G}_3^T \underline{d} = \sum_{i,j,k,l=1}^{n+1} \int\limits_{-1}^{+1}\int\limits_{-1}^{+1} \left[P_n''(\xi)P_n(\eta)L_i'(\xi)L_j(\eta)L_k'(\xi)L_l(\eta) - P_n(\xi)P_n''(\eta)L_i(\xi)L_j'(\eta)L_k(\xi)L_l'(\eta) \right] d\xi d\eta \cdot \underline{x}_{ij}^T \underline{u}_{kl}$$

$$= \sum_{i,j,k,l=1}^{n+1} \left(A_{ik}^2 A_{jl}^0 - A_{ik}^0 A_{jl}^2 \right) \cdot \underline{x}_{ij}^T \underline{u}_{kl} . \qquad (25)$$

In the above expressions,

$$A_{ij}^0 = \int\limits_{-1}^{+1} P_n(\xi)L_i(\xi)L_j(\xi)d\xi , \quad A_{ij}^1 = \int\limits_{-1}^{+1} P_n'(\xi)L_i'(\xi)L_j'(\xi)d\xi , \quad A_{ij}^2 = \int\limits_{-1}^{+1} P_n''(\xi)L_i'(\xi)L_j'(\xi)d\xi \qquad (26)$$

which are independent of the element geometry and can be pre-computed. Sub-parametric interpolations (i.e. the interpolation order of the coordinates is lower than that of the displacement) are commonly employed in high order elements. If they are employed, not more than six unsymmetric matrices will evolve but their dimensions would be smaller than those of the A-matrices.

On the other hand, provided that $\underline{\underline{H}}$ remains positively definite, patch test fulfillment will not be affected [16-18]. In this light, the approximations $J \simeq J\big|_{\xi=\eta=0}$ and $\underline{\underline{\tilde{S}}} \simeq \underline{\underline{\tilde{S}}}\big|_{\xi=\eta=0}$ are adopted for simplicity. Using the approximations and the proprieties of Legendre polynomial,

$$\underline{\underline{H}} \approx \frac{1}{J\big|_{\xi=\eta=0}} \begin{bmatrix} a\tilde{S}_{11}\big|_{\xi=\eta=0} & 0 & 0 \\ 0 & a\tilde{S}_{22}\big|_{\xi=\eta=0} & 0 \\ 0 & 0 & b(\tilde{S}_{11}+\tilde{S}_{22})\big|_{\xi=\eta=0} \end{bmatrix} = diag.\{h_1, h_2, h_3\} \qquad (27)$$

where

$$a = \int_{-1}^{+1} P_n'(\xi)P_n'(\xi)d\xi \cdot \int_{-1}^{+1} P_n(\xi)P_n(\xi)d\xi = \frac{2n(n+1)}{2n+1} \ , \ b = \int_{-1}^{+1} P_n''(\xi)P_n''(\xi)d\xi \cdot \int_{-1}^{+1} P_n(\xi)P_n(\xi)d\xi \ .$$

The zero variation of (24) with respect to $\underline{\beta}$ leads to $\underline{\underline{H}}\underline{\beta} = \underline{\underline{G}}\underline{d}.$ Thus,

$$\langle -\frac{1}{2}\underline{\sigma}_H^T \underline{\underline{C}}^{-1}\underline{\sigma}_H + \underline{\sigma}_H^T \underline{\varepsilon}\rangle^e = \frac{1}{2}\underline{d}^T \underline{\underline{G}}^T \underline{\underline{H}}^{-1}\underline{\underline{G}}\underline{d} \tag{28}$$

By back substituting (19) and (28) into (14), the latter reads

$$\Pi_{HR}^e = \frac{1}{2}\underline{d}^T (\underline{\underline{k}}_{URI} + \underline{\underline{G}}^T \underline{\underline{H}}^{-1}\underline{\underline{G}})\underline{d} - P^e \tag{29}$$

Discarding the stabilization vector $\underline{G}_3$, which stabilizes the incompatible zero energy mode, induces negligible change in the predictions for static problems. The fully and partially stabilized elements with three and two stabilization vectors will be abbreviated as FS and PS, respectively.

4.3 ORTHOGONALITY AND PATCH TEST

For the choice of the high order stress modes, the orthogonality condition stipulated in (13) can be expressed as:

$$\int_{-1}^{+1}\int_{-1}^{+1} G_i(\xi)G_j(\eta)\underline{\underline{C}}^{-1}\underline{\underline{T}}\begin{bmatrix} P_n'(\xi)P_n(\eta) & 0 & P_n''(\xi)P_n(\eta) \\ 0 & P_n(\xi)P_n'(\eta) & -P_n(\xi)P_n''(\eta) \\ 0 & 0 & 0 \end{bmatrix}d\xi d\eta = \underline{\underline{0}} \tag{30}$$

Noting that G_i and P_n are polynomials of order n-1 and n, respectively. As P_k is orthogonal to polynomials of order lower than k, the condition is exactly fulfilled for a constant $\underline{\underline{T}}$. For non-constant $\underline{\underline{T}}$, since P_n vanishes at RGQ points, the orthogonality is approximately satisfied when RGQ is employed.

For fulfillment of the constant stress patch test, the chosen high order stress modes need to be exactly orthogonal to constant stress modes, i.e.

$$\int_{-1}^{+1}\int_{-1}^{+1} \underline{\underline{T}}\begin{bmatrix} P_n'(\xi)P_n(\eta) & 0 & P_n''(\xi)P_n(\eta) \\ 0 & P_n(\xi)P_n'(\eta) & -P_n(\xi)P_n''(\eta) \\ 0 & 0 & 0 \end{bmatrix}d\xi d\eta = \underline{\underline{0}} \tag{31}$$

which can only be met for sub-parametric element geometry. For instance, the pertinent FS and PS element of order $n = 2$ can pass the constant stress patch test when the interpolated (x,y)-coordinates are bilinear in (ξ,η). To secure the patch test fulfillment, one can orthogonalize the stabilization vectors $\underline{G}_1$, $\underline{G}_2$ and $\underline{G}_3$ with respect to the $\underline{d}$'s arising from u, $v = 1$, x and y. However, our tests indicate that the change in the predication with and without the orthogonalization is negligible.

5. SELECTIVE REDUCED INTERATION

The SRI reviewed here is for alleviating dilatational locking [21, 36]. For nearly incompressible materials, the material stiffness matrix $\underline{\underline{C}}$ can often be expressed as:

$$\underline{\underline{C}} = \underline{\underline{D}} + \lambda \underline{m}^T \underline{m} \tag{32}$$

where $\underline{\underline{D}}$ is a diagonal matrix and $\underline{m} = [1,1,0]$. For instance, for plain strain isotropic materials,

$$\underline{\underline{D}} = \begin{bmatrix} 2\mu & 0 & 0 \\ 0 & 2\mu & 0 \\ 0 & 0 & \mu \end{bmatrix}, \quad \lambda = \frac{\upsilon E}{(1+\upsilon)(1-2\upsilon)} \quad \text{and} \quad \mu = \frac{E}{2(1+\upsilon)} \tag{33}$$

in which E is the elastic modulus and υ is the Poisson's ratio. By incorporating (32) into (4), the latter becomes

$$\Pi_P^e = \frac{1}{2} \langle \underline{\varepsilon}^T \underline{\underline{D}} \underline{\varepsilon} + \lambda (\underline{m}\underline{\varepsilon})^T \underline{m}\underline{\varepsilon} \rangle^e - P^e = \frac{1}{2} \langle \underline{\varepsilon}^T \underline{\underline{D}} \underline{\varepsilon} + \lambda \varepsilon_m^T \varepsilon_m \rangle^e - P^e \tag{34}$$

where $\varepsilon_m = \varepsilon_x + \varepsilon_y$ is the volumetric strain under the plain strain condition. By invoking (3),

$$\Pi_P^e = \frac{1}{2} \underline{d}^T (\langle \underline{\underline{B}}^T \underline{\underline{D}} \underline{\underline{B}} \rangle^e + \lambda \langle (\underline{m}\underline{\underline{B}})^T \underline{m}\underline{\underline{B}} \rangle^e) \underline{d} - P^e \tag{35}$$

For nearly incompressible materials, λ would be much large than entries in $\underline{\underline{D}}$ and may induce the well-known dilatational locking. A traditional way to alleviate the locking phenomenon without compromising the rank sufficiency of the finite element model is the SRI which employs full and reduced integrations to evaluate integrals of $\underline{\varepsilon}^T \underline{\underline{D}} \underline{\varepsilon}$ and $\varepsilon_m^T \varepsilon_m$, respectively. The stiffness matrix of the SRI model to be examined later in the numerical tests is

$$\underline{\underline{k}}_{SRI} = \langle \underline{\underline{B}}^T \underline{\underline{D}} \underline{\underline{B}} \rangle_{LBQ} + \lambda \langle (\underline{m}\underline{\underline{B}})^T \underline{m}\underline{\underline{B}} \rangle_{RGQ} \tag{36}$$

6. AXISYMMETRIC ELASTICITY

The stabilization vectors for axisymmetric elements can be derived in a manner similar to that of the plane elasticity. Axisymmetric problems are defined under the radial coordinate r and longitudinal coordinate z. The vectors of strain and stress components are:

$$\underline{\varepsilon} = \begin{Bmatrix} \varepsilon_r \\ \varepsilon_z \\ \gamma_{rz} \\ \varepsilon_\theta \end{Bmatrix} = \begin{bmatrix} \partial/\partial r & 0 \\ 0 & \partial/\partial z \\ \partial/\partial z & \partial/\partial r \\ 1/r & 0 \end{bmatrix} \begin{Bmatrix} u_r \\ u_z \end{Bmatrix} \quad , \quad \underline{\sigma} = \begin{Bmatrix} \sigma_r \\ \sigma_z \\ \sigma_{rz} \\ \sigma_\theta \end{Bmatrix} = \underline{\underline{C}} \underline{\varepsilon} \tag{37}$$

in which the elasticity matrix $\underline{C}$ is a 4×4. The element domain integral operator for axisymmetry is

$$\langle \circ \rangle^e = 2\pi \int_{-1}^{+1}\int_{-1}^{+1} \circ\, rJ d\xi d\eta \tag{38}$$

where the Jacobian determinant J becomes $(\partial r / \partial \xi)(\partial z / \partial \eta) - (\partial r / \partial \eta)(\partial z / \partial \xi)$. It is trivial to show that the spurious zero energy modes remain to be those expressed in (10). In analogy to (21) and (22), the contravariant high order stress modes are taken to be

$$\begin{Bmatrix} \sigma_\xi \\ \sigma_\eta \\ \sigma_{\xi\eta} \\ \sigma_\theta \end{Bmatrix} = \frac{1}{rJ}\begin{bmatrix} P_n'(\xi)P_n(\eta) & 0 & P_n''(\xi)P_n(\eta) \\ 0 & P_n(\xi)P_n'(\eta) & -P_n(\xi)P_n''(\eta) \\ 0 & 0 & 0 \\ 0 & 0 & 0 \end{bmatrix}\underline{\beta} = \frac{1}{rJ}\underline{\underline{P}}\underline{\beta} \tag{39}$$

and its physical counterpart can be obtained as:

$$\underline{\sigma}_H = \begin{bmatrix} r_{,\xi}\, r_{,\xi} & r_{,\eta}\, r_{,\eta} & 2r_{,\xi}\, r_{,\eta} & 0 \\ z_{,\xi}\, z_{,\xi} & z_{,\eta}\, z_{,\eta} & 2z_{,\xi}\, z_{,\eta} & 0 \\ r_{,\xi}\, z_{,\xi} & r_{,\eta}\, z_{,\eta} & r_{,\xi}\, z_{,\eta} + z_{,\xi}\, r_{,\eta} & 0 \\ 0 & 0 & 0 & 1 \end{bmatrix}\begin{Bmatrix} \sigma_\xi \\ \sigma_\eta \\ \sigma_{\xi\eta} \\ \sigma_\theta \end{Bmatrix} = \frac{1}{rJ}\underline{\underline{T}}\,\underline{\underline{P}}\,\underline{\beta} \tag{40}$$

The stabilization vectors and *H*-matrix for the axisymmetric elements are similar to those of the plane elements, see (25) and (27), except that $\underline{x}_{ij}$, $\underline{u}_{kl}$ and $J\big|_{\xi=\eta=0}$ for the plane elements become $\underline{x}_{ij} = \{r_{ij}, z_{ij}\}^T$, $\underline{u}_{kl} = \{u_{rkl}, u_{zkl}\}^T$ and $(rJ)\big|_{\xi=\eta=0}$, respectively. Furthermore, the vectors and matrix for the axisymmetric elements should contain the multiplier 2π.

7. NUMERICAL TESTS

Numerical tests are conducted to examine the accuracy and convergence of the following element models with different order *n*:

- LB: the standard Lobatto element integrated by the LBQ, see (7)
- SRI: the selective reduced integration element, see (36)
- PS: the partially stabilized element with two stabilization vectors, see (29)
- FS: the fully stabilized element with three stabilization vectors, see (29)

The following relative displacement error integrated by LBQ and the relative energy error integrated by RGQ will be employed to quantify the element accuracy:

$$\text{relative displacement error} = \left[\frac{\sum_e \left\langle (\underline{u} - \underline{u}^{exact})^T (\underline{u} - \underline{u}^{exact}) \right\rangle_{LBQ}}{\sum_e \left\langle (\underline{u}^{exact})^T \underline{u}^{exact} \right\rangle_{LBQ}} \right]^{\frac{1}{2}},$$

$$\text{relative energy error} = \left[\frac{\sum_e \left\langle (\underline{\sigma} - \underline{\sigma}^{exact})^T \underline{\underline{C}}^{-1} (\underline{\sigma} - \underline{\sigma}^{exact}) \right\rangle_{RGQ}}{\sum_e \left\langle (\underline{\sigma}^{exact})^T \underline{\underline{C}}^{-1} \underline{\sigma}^{exact} \right\rangle_{RGQ}} \right]^{\frac{1}{2}}. \tag{41}$$

The latter is often referred to as relative error in energy norm. The integration rules are chosen as displacement and stress predictions are well-known to be most accurate at the nodes and RGQ points. In all problems, the results of PS and FS element are graphically indistinguishable and only those of PS element will be presented for clarity.

7.1 Panel with a Circular Cutout

A plane strain panel with a unit radius circular cutout is considered [12, 37]. Due to symmetry, only one-quarter of the panel is modeled as shown in Figure 4. Except those around the circular cutout, all elements are bilinear in geometry. Along $x = 4$ and $y = 4$, tractions are prescribed according to

$$\underline{\sigma}^{exact} = \left\{ \begin{array}{c} \sigma_x^{exact} \\ \sigma_y^{exact} \\ \sigma_{xy}^{exact} \end{array} \right\} = \left\{ \begin{array}{c} 1 \\ 0 \\ 0 \end{array} \right\} - \frac{1}{2r^2} \left\{ \begin{array}{c} 3\cos 2\theta + 2\cos 4\theta \\ \cos 2\theta - 2\cos 4\theta \\ \sin 2\theta + 2\sin 4\theta \end{array} \right\} + \frac{3}{2r^4} \left\{ \begin{array}{c} \cos 4\theta \\ -\cos 4\theta \\ \sin 4\theta \end{array} \right\} \tag{42}$$

which is the stress solution for an infinite plate with a unit radius circular hole subjected to far field traction $\sigma_x = 1$. The corresponding displacement solution is

$$\underline{u}^{exact} = \left\{ \begin{array}{c} u^{exact} \\ v^{exact} \end{array} \right\} = \frac{r}{8\mu} \left\{ \begin{array}{c} (k+1)\cos\theta \\ (k-3)\sin\theta \end{array} \right\} + \frac{1}{4\mu r} \left\{ \begin{array}{c} (1+k)\cos\theta + \cos 3\theta \\ (1-k)\sin\theta + \sin 3\theta \end{array} \right\} - \frac{1}{4\mu r^3} \left\{ \begin{array}{c} \cos 3\theta \\ \sin 3\theta \end{array} \right\} \tag{43}$$

where $k = 3 - 4\upsilon$. In the *h*-refinement, meshes of $m \times 2m$ elements are employed where $m = 1, 2, 4$ and 8. Errors of LB, PS and SRI of orders $n = 2, 4$ and 6 are compared in Figures 5(a), 5(b) and 5(c), respectively, for $\upsilon = 0.25$ and $\upsilon = 0.4999$. For $\upsilon = 0.25$, PS is the most and least accurate element model regardless of the element order in view of the displacement and energy errors whilst the predictions of LB and SRI are close. For $\upsilon = 0.4999$, the predictions of PS and SRI deteriorate mildly whilst those of LB worsen significantly. Figure 5(d) shows the convergence of the *p*-refinement for which the 1×2 mesh is employed. The relative accuracy of the elements is the same as that observed in the *h*-refinement.
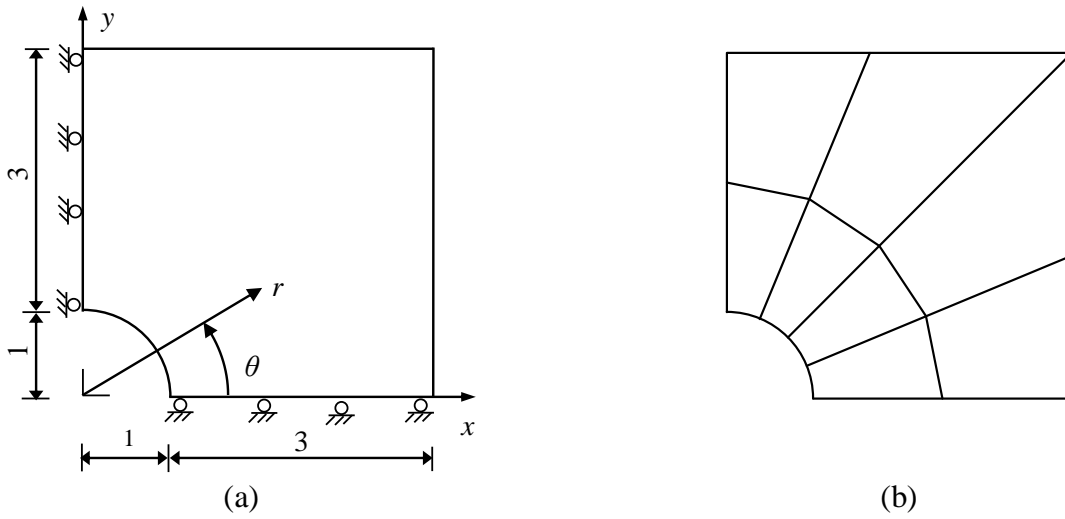
Figure 4. (a) Square panel with a circular cutout. (b) The 2×4 mesh. Along $x = 4$ and $y = 4$, tractions are prescribed according to the analytical solution.
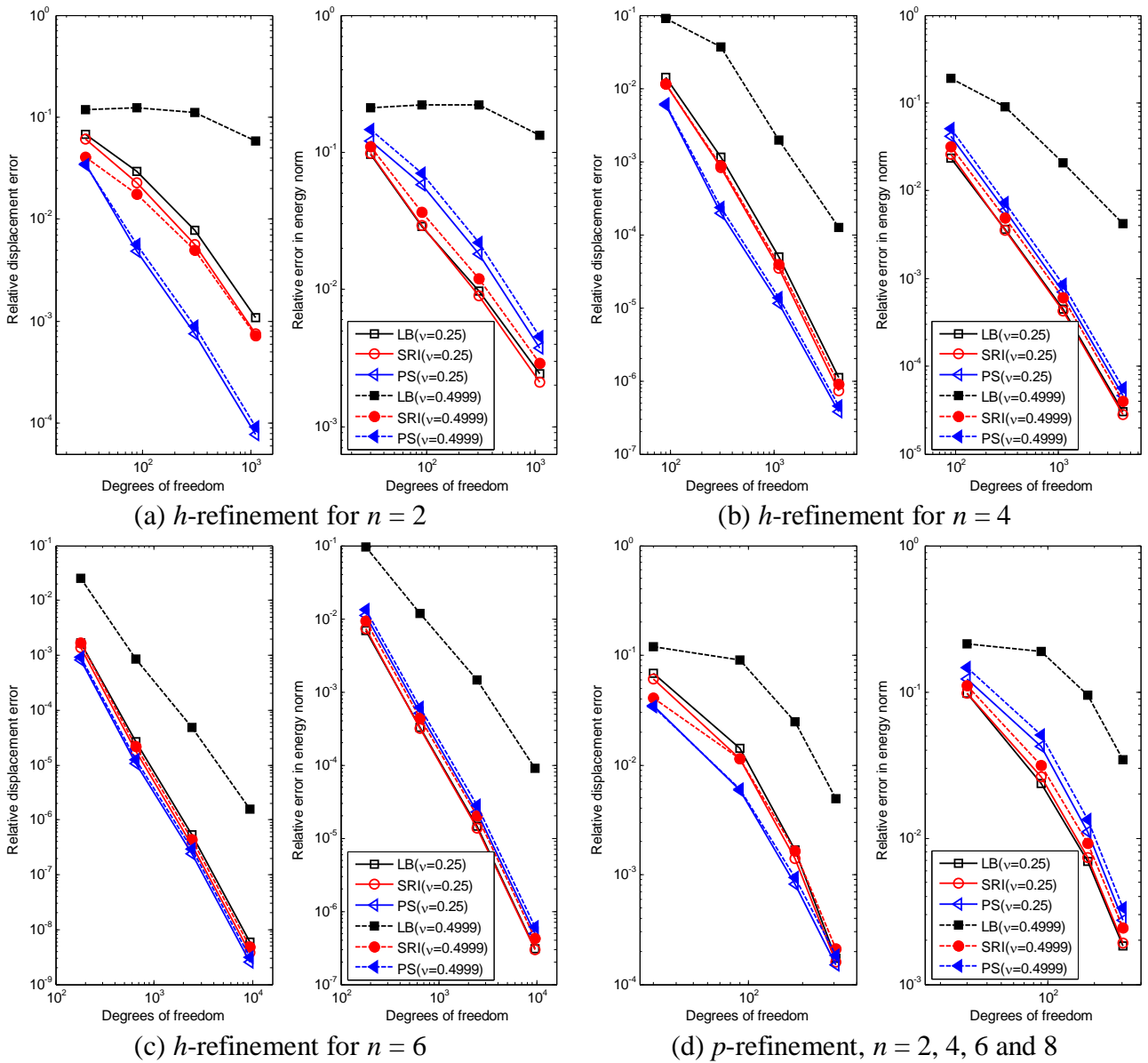

(a) *h*-refinement for $n = 2$

(b) *h*-refinement for $n = 4$

(c) *h*-refinement for $n = 6$

(d) *p*-refinement, $n = 2$, 4, 6 and 8

Figure 5. Relative displacement and energy errors for the square panel problem.

7.2 Cylinder under Internal Pressure

This example considers a plane strain thick-walled cylinder with inner radius a and outer radius b equal to 5 and 20 units, respectively. Owing to symmetry, only a quarter of the cylinder is modelled. The internal surface is subjected to a uniform pressure P and the outer surface is traction-free, see Figure 6(a). The analytical displacement and stress solutions are [38]:

$$\underline{u}^{exact} = \begin{Bmatrix} u^{exact} \\ v^{exact} \end{Bmatrix} = \frac{1+\upsilon}{E} \frac{Pa^2 r}{b^2 - a^2} (\frac{b^2}{r^2} + 1 - 2\upsilon) \begin{Bmatrix} \cos\theta \\ \sin\theta \end{Bmatrix},$$

$$\underline{\sigma}^{exact} = \begin{Bmatrix} \sigma_x^{exact} \\ \sigma_y^{exact} \\ \sigma_{xy}^{exact} \end{Bmatrix} = \frac{a^2 P}{b^2 - a^2} (\begin{Bmatrix} 1 \\ 1 \\ 0 \end{Bmatrix} + \frac{b^2}{r^2} \begin{Bmatrix} -\cos 2\theta \\ \cos 2\theta \\ -\sin 2\theta \end{Bmatrix}) . \tag{44}$$

The h-convergence of the elements is investigated by using meshes with $m \times m$ elements where $m = 1, 2, 4$ and 8, see Figure 6(b). Figures 7(a), 7(b) and 7(c) shows the errors for $n = 2, 4$ and 6, respectively. It can be seen that PS yields distinctively better displacement predictions than the other elements for both $\upsilon = 0.25$ and $\upsilon = 0.4999$. In the energy error, the results of LB, SRI and PS are graphically indistinguishable when $\upsilon = 0.25$. Same as the last example, both the displacement and energy errors of LB severely deteriorate when $\upsilon = 0.4999$. On the other hand, the accuracy of SRI and PS are basically unaffected by the change of Poison's ratio. Note worthily, the displacement convergence of PS ($n = 6$) slows down and even reverse in Figure 7(c). The abnormality can be rectified by using quad precision which leads to the results denoted by "*"and, thus, is caused by round-off error. Using the single-element mesh, the p-convergence can be seen in Figure 7(d). The relative accuracy of the elements is the same as that shown in the h-convergence.
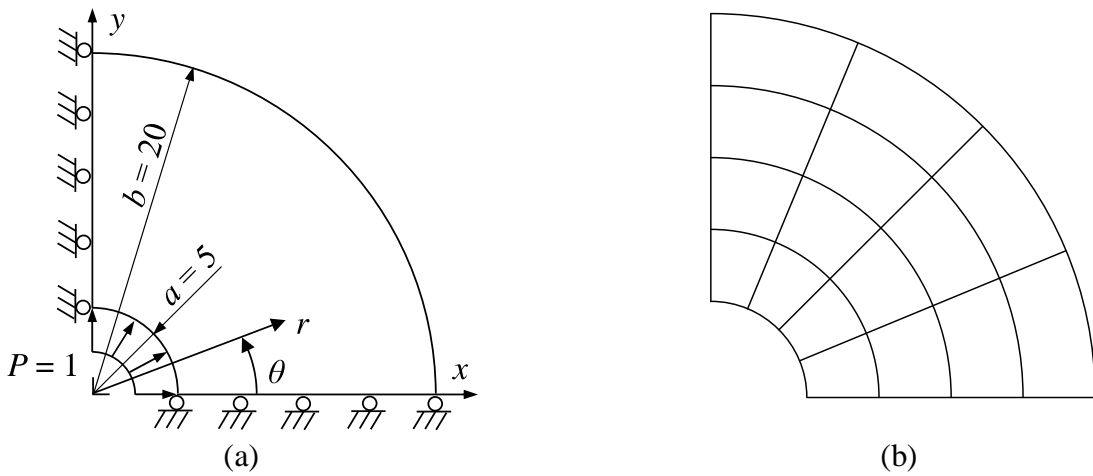

Figure 6. (a) Thick cylinder under internal pressure. (b) The 4×4 mesh.

(a) *h*-refinement for *n* = 2

(b) *h*-refinement for *n* = 4

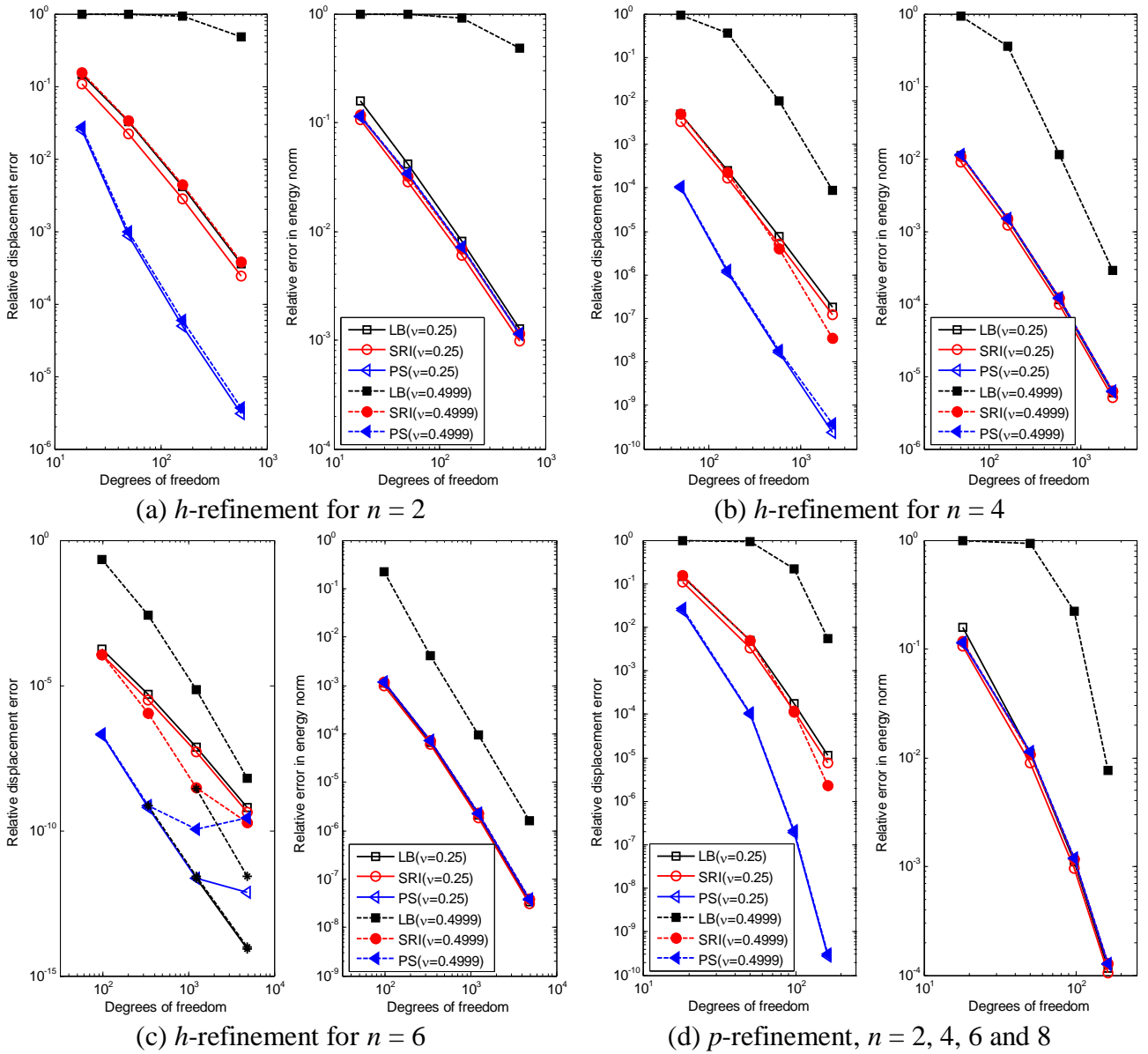(c) *h*-refinement for *n* = 6

(d) *p*-refinement, *n* = 2, 4, 6 and 8

Figure 7. Relative displacement and energy errors for the thick cylinder problem. In (c), * denotes the predictions of SRI and PS obtained by quad precision.

7.3 Non-leaky Cavity Problem

This is a challenging problem against dilatational locking [25, 29, 39]. It considers a plain strain square domain. The bottom, left and right edges are fully restrained whilst all except the two corner nodes on the top edge side are prescribed with 10^{-3} tangential and zero normal displacements, as shown in Figure 8. The material properties include $E = 10^6$ and $\upsilon = 0.4999$. In addition to the displacements, the mean stress, $\sigma_m = (\sigma_x + \sigma_y + \sigma_z)/3 = (\sigma_x + \sigma_y)(1 + \upsilon)/3$, is of interest in this problem. A mesh of 7×7 elements is adopted and elements of order $n = 2$ and 4 are examined.

Displacements along $y = 0$ predicted by elements of order $n = 2$ and 4 are presented in Figures 9(a) and 9(b), respectively. The *x*-displacement predictions of SRI and PS exhibit oscillations but

that of LB is smooth. On the contrary, the *y*-displacement predictions of SRI and PS are smooth but that of LB oscillates in the vicinity of the domain boundary.
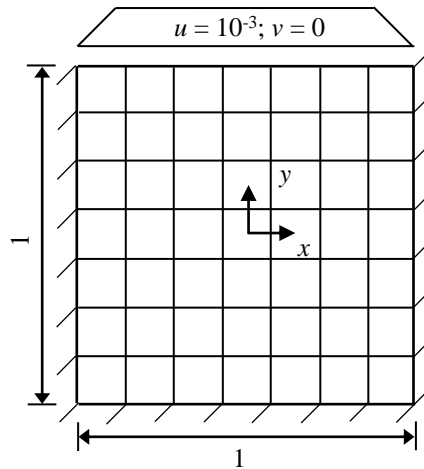

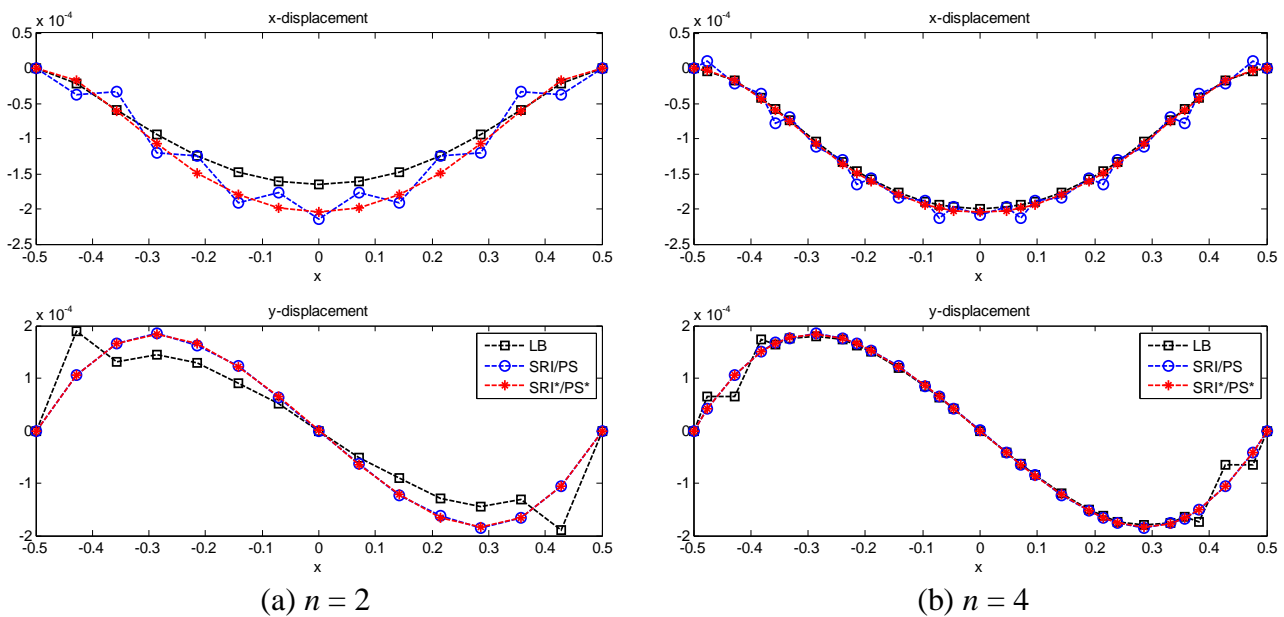Figure 8. The non-leaky cavity problem with 7×7-element mesh.

(a) $n = 2$
(b) $n = 4$

Figure 9. Displacement predictions along the line $y = 0$.

The σ_m-predictions along the row of RGQ points immediately above $y = 0$ are shown in Figures 10(a) and 10(b) for $n = 2$ and 4, respectively. For $n = 2$, the predictions of SRI and PS oscillate between ±16,000 whilst that of LB oscillates between ±5,000. For $n = 4$, there is not much improvement for SRI and PS but the oscillation in the prediction of LB has been greatly reduced.
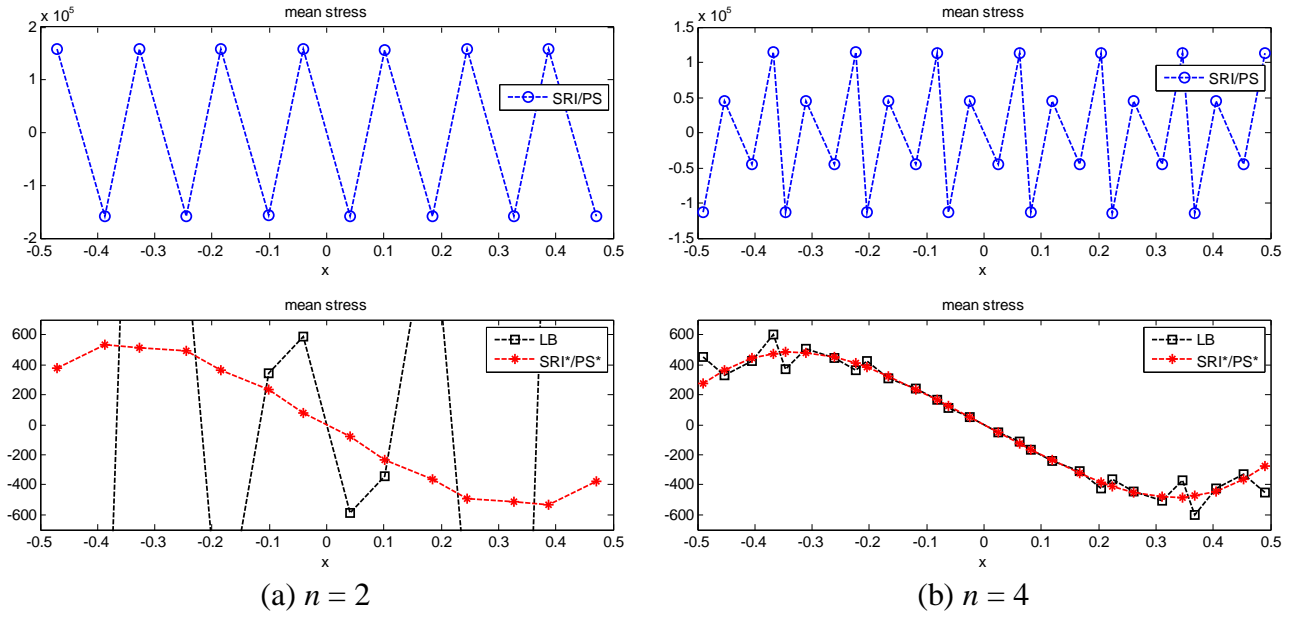
(a) $n = 2$

(b) $n = 4$

Figure 10. Mean stress predictions along the row of reduced Gaussian points immediately above $y = 0$.

7.4 Rank Reduction for Zero Dilation Constraint Matrix

For SRI and PS, the stress oscillation reported in the last example is caused by the excessive rank of the matrix $\langle (m\underline{\underline{B}})^T m\underline{\underline{B}} \rangle_{RGQ}$ in (36) which enforces the zero dilatation condition, i.e. $\varepsilon_m = 0$, at the RGQ points. A rank reduction technique has been developed in [25]. It can be implemented by augmenting the volumetric strain $m\underline{\underline{B}}\underline{d}$ with the rank subtraction modes $\underline{\underline{E}}\underline{\varphi}$, i.e.

$$\varepsilon_m = m\underline{\underline{B}}\underline{d} + \underline{\underline{E}}\underline{\varphi} \tag{45}$$

in which $\underline{\underline{E}}$ is the shape function row matrix and $\underline{\varphi}$ is the vector of coefficients. Taking the element potential of the SRI element in (36) as an example, the new energy potential is

$$\Pi_{mP}^e = \frac{1}{2}\underline{d}^T \langle \underline{\underline{B}}^T \underline{\underline{D}}\underline{\underline{B}} \rangle_{LBQ} \underline{d} + \frac{\lambda}{2} \left\{ \begin{matrix} \underline{d} \\ \underline{\varphi} \end{matrix} \right\}^T \begin{bmatrix} \langle (m\underline{\underline{B}})^T m\underline{\underline{B}} \rangle_{RGQ} & \langle (m\underline{\underline{B}})^T \underline{\underline{E}} \rangle_{RGQ} \\ \langle (m\underline{\underline{B}})^T \underline{\underline{E}} \rangle_{RGQ}^T & \langle \underline{\underline{E}}^T \underline{\underline{E}} \rangle_{RGQ} \end{bmatrix} \left\{ \begin{matrix} \underline{d} \\ \underline{\varphi} \end{matrix} \right\} - P^e \tag{46}$$

Then, $\underline{\varphi}$ is condensed using the zero variation of $\underline{\varphi}$, i.e. $\langle (m\underline{\underline{B}})^T \underline{\underline{E}} \rangle_{RGQ}^T \underline{d} + \langle \underline{\underline{E}}^T \underline{\underline{E}} \rangle_{RGQ} \underline{\varphi} = \underline{0}$, and

$$\Pi_{mP}^e = \frac{1}{2}\underline{d}^T \left(\langle \underline{\underline{B}}^T \underline{\underline{D}}\underline{\underline{B}} \rangle_{LB} + \lambda \langle (m\underline{\underline{B}})^T m\underline{\underline{B}} \rangle_{RGQ} - \lambda \langle (m\underline{\underline{B}})^T \underline{\underline{E}} \rangle_{RGQ} \langle \underline{\underline{E}}^T \underline{\underline{E}} \rangle_{RGQ}^{-1} \langle (m\underline{\underline{B}})^T \underline{\underline{E}} \rangle_{RGQ}^T \right) \underline{d} - P^e \tag{47}$$

It should be remarked that the rank reduction technique is fundamentally different from EAS (enhanced assumed strain) method [30]. In the former, $\underline{\underline{E}}$ must be a subset of $m\underline{\underline{B}}$ such that

$$\text{rank}\left(\langle (m\underline{\underline{B}})^T m\underline{\underline{B}} \rangle_{RGQ} - \langle (m\underline{\underline{B}})^T \underline{\underline{E}} \rangle_{RGQ} \langle \underline{\underline{E}}^T \underline{\underline{E}} \rangle_{RGQ}^{-1} \langle (m\underline{\underline{B}})^T \underline{\underline{E}} \rangle_{RGQ}^T \right) < \text{rank}\left(\langle (m\underline{\underline{B}})^T m\underline{\underline{B}} \rangle_{RGQ} \right).$$

On the other hand, the bases of strain modes arising from the nodal displacement and the enhancing modes in EAS must be mutually exclusive. Numerical trials show that the follow rank reduction

mode can eliminate the displacement and stress oscillation in the non-leaky cavity problem:

$$\underline{\underline{E}} = \frac{1}{J}\left[P_{n-1}(\xi)P_{n-1}(\eta)\right] \tag{48}$$

The predictions of the SRI and PS elements with the rank subtraction mode incorporated are labeled as SRI* and PS* in Figures 9 and 10. It can be seen that the displacement and mean stress oscillations are successfully eliminated. Moreover, displacement predictions of LB ($n = 2$) is overly stiff compared with those of SRI* and PS*.

7.5 Maximum Eigen Frequencies for Square Elements with Lobatto and Equispaced Nodes

It is well-known that explicit time integration is conditionally stable and require the time increment to be smaller than the critical time step $\Delta t_c = 2/\Omega_{max}$ in which Ω_{max} is the maximum eigen frequency of the system. On the other hand, Ω_{max} is bounded by the maximum element eigen frequency ω_{max}, given in $\underline{k}\underline{d} = \omega^2 \underline{m}\underline{d}$ where $\underline{m} = \langle \rho \underline{N}^T \underline{N} \rangle^e$ is the element mass matrix and ρ is the material density, among the elements in the system [36]. The maximum element eigen frequency is often used to estimate the allowable time increment for stable prediction. In this example, the maximum eigen frequencies of square elements with different combinations of nodal distribution (Lobatto and equispaced nodes), mass matrices (evaluated by LBQ, full order Gaussian quadrature or FGQ, LBQ plus diagonalization and FGQ plus diagonalization) and stiffness matrices (evaluated by LBQ and SRI, stabilized by PS). The diagonalization of the mass matrix is attained by row summation that lumps all entries in the same matrix row as well as replaces the diagonal and off-diagonal entries by the lumped sum and zeros, respectively [36]. For $\upsilon = 0.25$ or 0.4999, the normalized maximum eigenfrequency $\omega_{max}L\sqrt{(\rho/E)}$ which is independent of E, ρ and the element side length L are shown in Tables 1a, 1b and 1c for element order $n = 2$, 4 and 6, respectively. For $n = 2$, Lobatto and equispaced nodes are identical. Hence, they are not distinguished in Table 1a. As interpolation bases of the Lobatto and equispaced nodes are identical, the maximum frequencies should not change with the nodal distribution. Thus, the predictions for (1) and (2) are identical to those of (4) and (5), respectively, in Tables 1b and 1c. The equivalence between (1) and (3) as well as the equivalence between (6) and (7), if any, in each of the tables are rather unexpected. However, the equivalence of the pertinent mass matrices can indeed be proven for regular elements as follows. The i-th row of the mass matrix is $\underline{m} = \langle \rho N_i \underline{N} \rangle^e$. By invoking the partition of unity, the sum of the entries in the i-th row is:

$$\left\langle \rho N_i \sum_{j=1}^{n+1} N_j \right\rangle^e = \left\langle \rho N_i \right\rangle^e.$$

As both LBQ and FGQ can exactly integrate N_i, the equivalence follows.

Though FGQ is more accurate than LBQ, FGQ-evaluated mass matrices lead to higher maximum element eigenfrequencies than LBQ-evaluated ones and, thus, impose smaller critical time steps in the explicit time integration. Furthermore, the maximum element eigenfrequencies arising from LBQ-evaluated mass matrices are insensitive to the element stiffness matrix formulation whilst those arising from FGQ-evaluated mass matrices vary considerably.

Table 1a. The maximum normalized eigenfrequencies $\omega_{max}L\sqrt{(\rho/E)}$ for elements of order $n = 2$.

m	*k*	$\upsilon = 0.25$	$\upsilon = 0.4999$
(1) Diagonal, by LBQ rule	LB	6.57	282.86
	SRI	6.57	282.86
	PS	6.20	282.85
(2) Non-diagonal, by FGQ rule	LB	15.49	500.12
	SRI	13.42	447.24
	PS	9.80	447.23
(3) Diagonal, by FGQ rule + diagonalization	Remark: Same as (1).		

Table 1b. The maximum normalized eigenfrequencies $\omega_{max}L\sqrt{(\rho/E)}$ for elements of order $n = 4$.

Node	*m*	*k*	$\upsilon = 0.25$	$\upsilon = 0.4999$
Lobatto ($n = 4$)	(1) Diagonal, by LBQ	LB	18.86	781.82
		SRI	18.86	781.82
		PS	18.08	781.80
	(2) Non-diagonal, by FGQ	LB	36.72	1194.37
		SRI	31.80	1125.89
		PS	24.80	1125.85
	(3) Diagonal, by FGQ + diagonalization	Remark: Same as (1).		
Equispaced ($n = 4$)	(4) Non-diagonal, by LBQ	Remark: Same as (1).		
	(5) Non-diagonal, by FGQ	Remark: Same as (2).		
	(6) Diagonal, by LBQ + diagonalization	LB	38.14	1277.09
		SRI	35.32	978.95
		PS	29.46	978.87
	(7) Diagonal, by FGQ + diagonalization	Remark: Same as (6).		

Table 1c. The maximum normalized eigenfrequencies $\omega_{max}L\sqrt{(\rho/E)}$ for elements of order $n = 6$.

Node	*m*	*k*	$\upsilon = 0.25$	$\upsilon = 0.4999$
Lobatto	(1) Diagonal, by LBQ	LB	38.51	1580.77

(*n* = 6)		SRI	38.51	1580.77
		PS	37.46	1580.75
	(2) Non-diagonal, by FGQ	LB	65.69	2170.95
		SRI	56.91	2085.50
		PS	46.51	2085.43
	(3) Diagonal, by FGQ + diagonalization	Remark: Same as (1).		
Equispaced (*n* = 6)	(4) Non-diagonal, by LBQ	Remark: Same as (1).		
	(5) Non-diagonal, by FGQ	Remark: Same as (2).		
	(6) Diagonal, by LBQ + diagonalization	LB	393.56	12778.31
		SRI	363.37	8433.42
		PS	296.74	8431.98
	(7) Diagonal, by FGQ + diagonalization	Remark: Same as (6).		

The results to be discussed and presented from now on are restricted to Lobatto elements, i.e. using the Lobatto nodes and LBQ-evaluated mass matrices. From Tables 1(a), (b) and (c), one can see that the normalized maximum eigenfrequencies $\omega_{\max}L\sqrt{(\rho/E)}$ increase more than linearly with *n*. Moreover, the element length *L* equals *n* times average nodal spacing. Thus, at the same average nodal spacing, high order elements impose smaller critical time steps than the low order elements. However, this drawback of the high order elements on the computational efficiency may possibly be offset by the higher accuracy of the elements.

7.6 Normalized Element Eigenfrequencies

Figure 11 shows the normalized element eigenfrequencies $\omega L\sqrt{(\rho/E)}$ in increasing order of LB, SRI and PS for *n* = 2, 4 and υ = 0.25, 0.4999. For υ = 0.25, all the normalized eigenfrequencies are less than 20 whilst the eigenfrequencies yielded by LB are marginally higher than those of SRI which are, in turn, marginally higher than those of PS. For υ = 0.4999, LB, SRI and PS of *n* = 2 (*n* = 4) possess respectively 8, 4 and 4 (24, 16 and 16) normalized eigenfrequencies which are larger than 100. The numbers are largely consistent with the number of integration points used in evaluating the dilatational energy in the elements. At the two ends of the frequency range, the eigenfrequencies predicted by LB, SRI and PS are graphically indistinguishable.
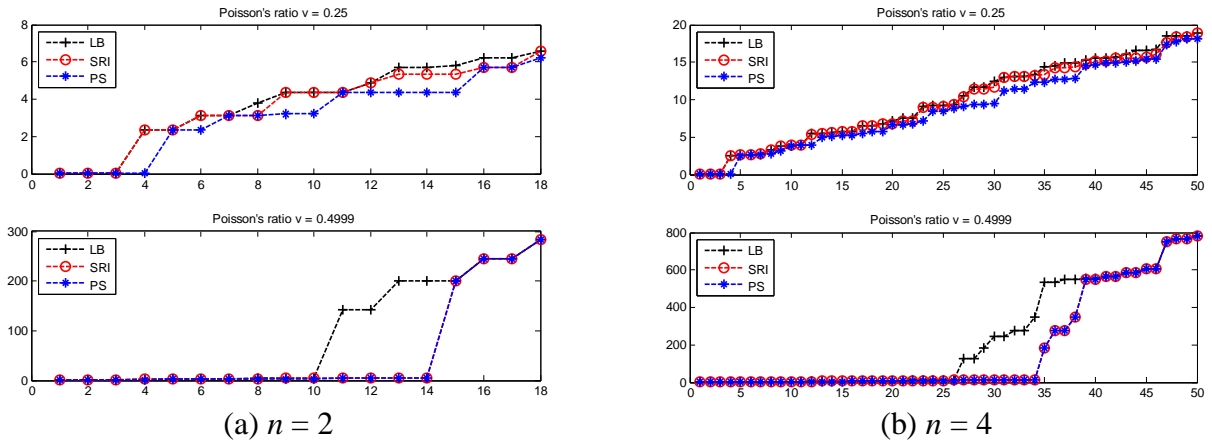
Figure 11. Normalized element eigenfrequencies $\omega L\sqrt{(\rho/E)}$ in increasing order for $n = 2$ and 4.

7.7 Wave Propagation Problem 289×289 Nodes

In this section, wave propagation in a 5760×2880 rectangular domain is investigated [3, 40], see Figure 12. The bottom and vertical edges are full constrained whilst the top edge is free. Owing to symmetry, only the half domain at $x > 0$ is modeled. The following Ricker wavelet source is applied to the coordinate origin in the form of a point force along the y-axis:

$$F_y = -10^6 \times \left(1 - 2\pi^2 f_0^2 (t - t_0)^2\right) \exp\left(-\pi^2 f_0^2 (t - t_0)^2\right) \quad \text{for} \ \ t > 0$$

where $f_0 = 12.5$ and $t_0 = 0.1$. Figure 13 shows F_y versus t and the Fourier transform of F_y versus frequency f. It can see seen that the excitation force becomes essentially zero after $t = 0.2$. The Fourier transform peaks at $f = f_0$ and its amplitude at frequency larger than $2.5f_0$ is less than 5% of the peak value. Two receivers are placed at $x = 480$ and $x = 960$ as shown. The material properties include $E = 18.773 \times 10^9$, $\rho = 2200$ and $\upsilon = 0.25$ or 0.4999. Regular elements of order $n = 2$, 3 and 4 are examined and the number of nodes is kept at 289×289, i.e. the average nodal spacing is 10. In other words, there would be 72×72 fourth order elements. On the other hand, a mesh with 288×288 fourth order elements with average nodal spacing at 2.5 is also set up for providing the reference solution. The standard central difference method is used for time integration. The estimated critical time step increment ($= 2/\omega_{max}$) for the given material properties and element sizes are listed in the last two columns of Table 2. Same as the observation in Section 6.5, the increment drops as the element order goes up.
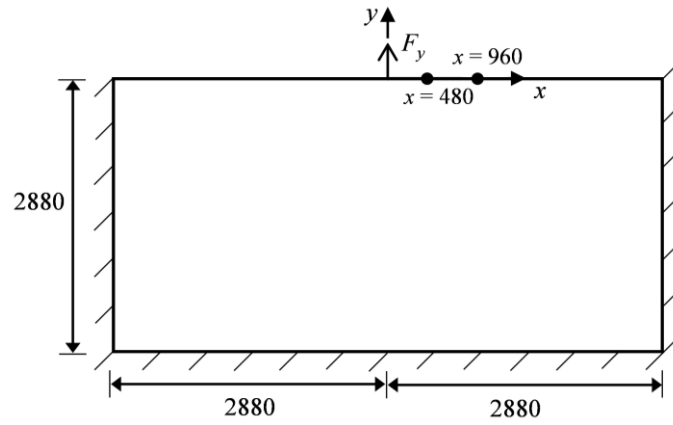
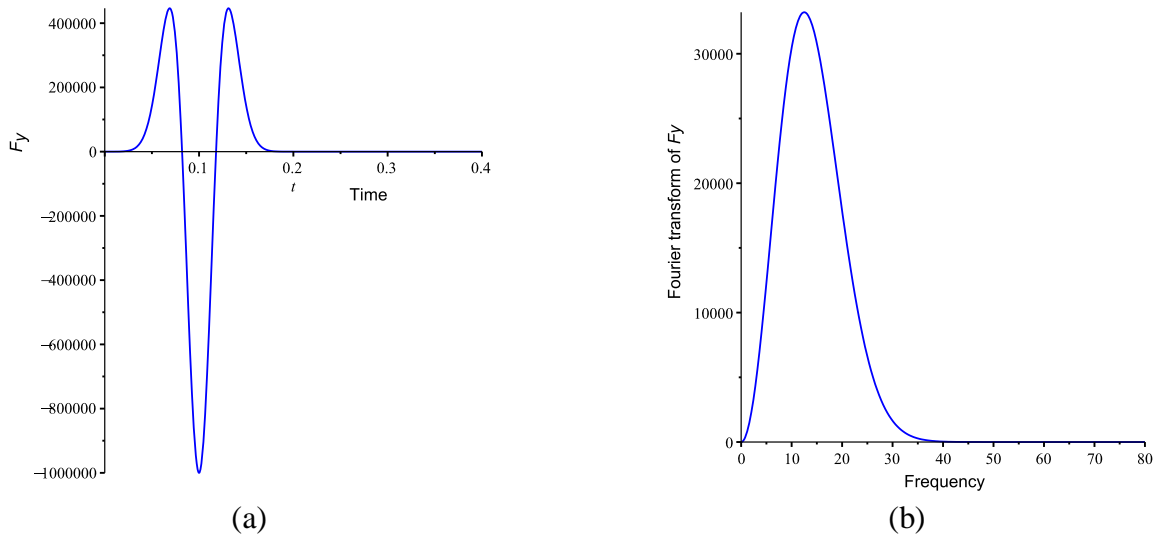Figure 12. The rectangular domain for wave propagation.

Figure 13. F_y in (a) time domain and (b) frequency domain.

Table 2. The estimated critical time step increment for second, third and fourth order elements.

Element order	Average nodal spacing	$\upsilon = 0.25$	$\upsilon = 0.4999$
2	10	2.083×10^{-3}	48.41×10^{-6}
3	10	1.732×10^{-3}	41.27×10^{-6}
4	10	1.452×10^{-3}	35.03×10^{-6}
4 (for reference solution)	2.5	363.0×10^{-6}	8.757×10^{-6}

The speeds of the pressure (P), shear (S) and Rayleigh (R) waves [41] are related to the material properties as

$$V_P = \sqrt{\frac{\lambda + 2\mu}{\rho}} \ , \quad V_S = \sqrt{\frac{\mu}{\rho}} \ \text{ and } \ V_R \approx \frac{0.862 + 1.14\upsilon}{1+\upsilon} V_S \tag{49}$$

When the Poisson's ratio equals 0.25, V_P (= 3200) nearly doubles V_S (= 1848) and V_R (= 1695). At frequency $2.5f_0$, the wavelength of the R-waves is $V_R/(2.5f_0) = 54.25$ and the number of nodes

per wavelength is $54.25/10 \approx 5.4$ which appears to be marginally for second order elements but fine for high order elements. The numbers of nodes per wavelength for the P- and S-waves are ≈ 10 and ≈ 6, respectively. For all elements, the time step increment are taken to be 10^{-3} which is approximately 70% of the estimated critical time step increment of the fourth order element given in Table 2. Figure 14 shows the time histories of the y-displacement predicted by elements with order $n = 2$, 3 and 4 at the positions of the two receivers. The results of LB, SRI, PS and FS are all very close to the reference solution obtained by the 288×288 fourth order elements and time step increment 100×10^{-6}. Figure 15 portrays the reference solutions for the (a) deviatoric and (b) dilatational energy density distributions at $t = 0.8$. These plots are based on the deviatoric energy density ($= \underline{\varepsilon} \underline{\underline{D}} \underline{\varepsilon} / 2$ where $\varepsilon = \underline{\underline{B}} \underline{d}$) and ($\lambda \varepsilon_m^2 / 2$ where $\varepsilon_m = \underline{m} \underline{\varepsilon}$) computed at the RGQ points. Predictions by LB, SRI, PS and FS are graphically indistinguishable from the reference solutions and, thus, are not repeated. Three groups of waves can be noted in the deviatoric energy plot in Figure 15(a). The waves localized at the surface have high intensity and should be the R-waves. The ones below and marginally faster than the R-waves should be the S-waves which also possess high intensity. The ones about one time farther away from the excitation source than the S-wave should be the P-waves which are very low in intensity and diminish gradually towards the traction-free surface. Figure 15(b) shows the dilatational energy plot. The area occupied by the P-waves in deviatoric energy plot in Figure 15(a) is occupied by distinctive fringes in the dilatational energy plot in Figure 15(b). From the two energy plots, it can be seen that the peak deviatoric energy density is one order of magnitude higher than the peak dilatational energy density.
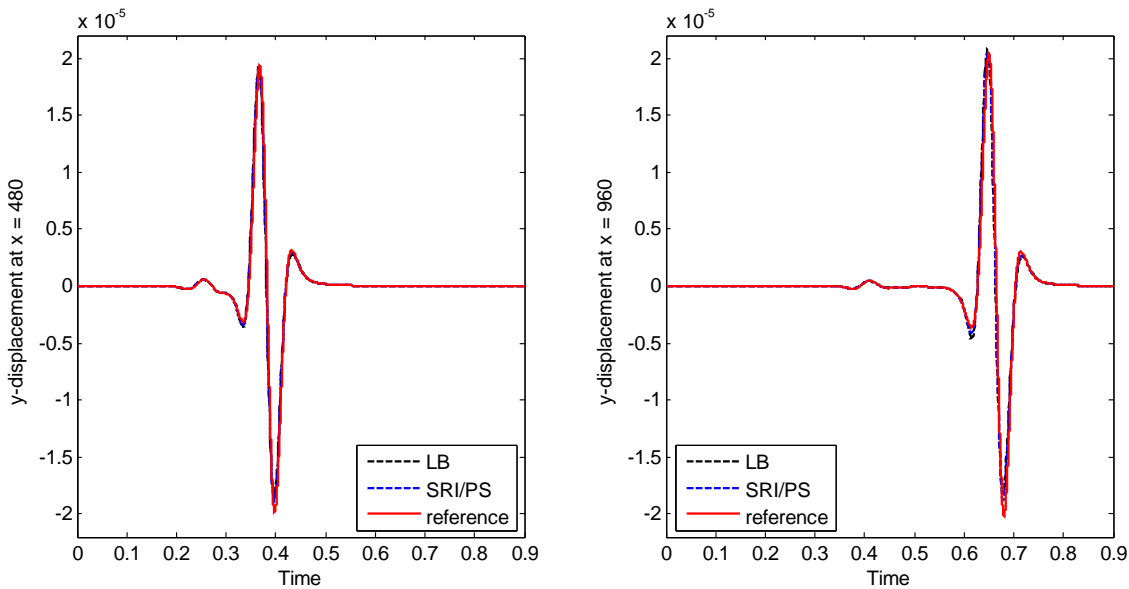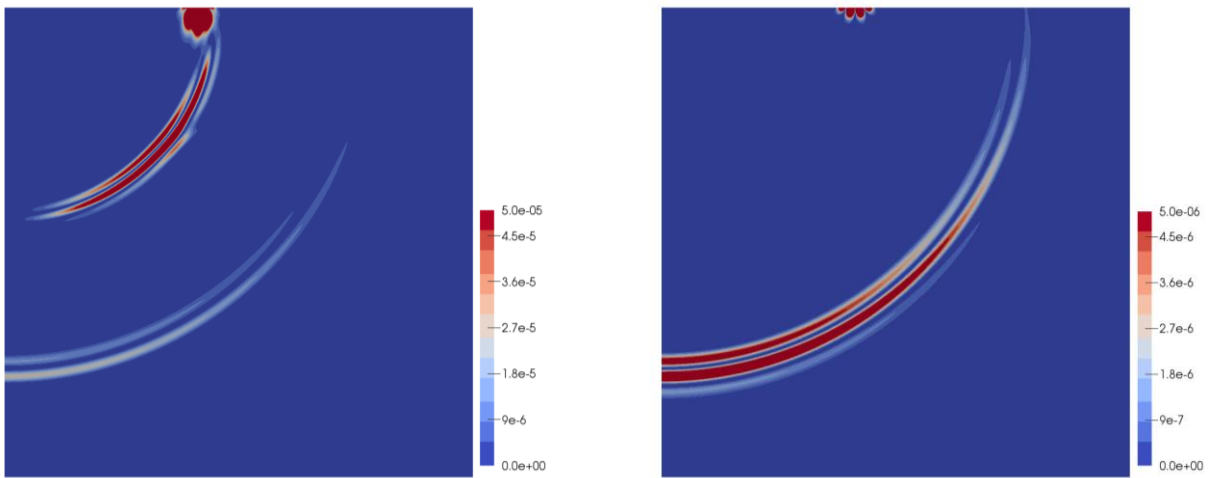

(a) $n = 2$
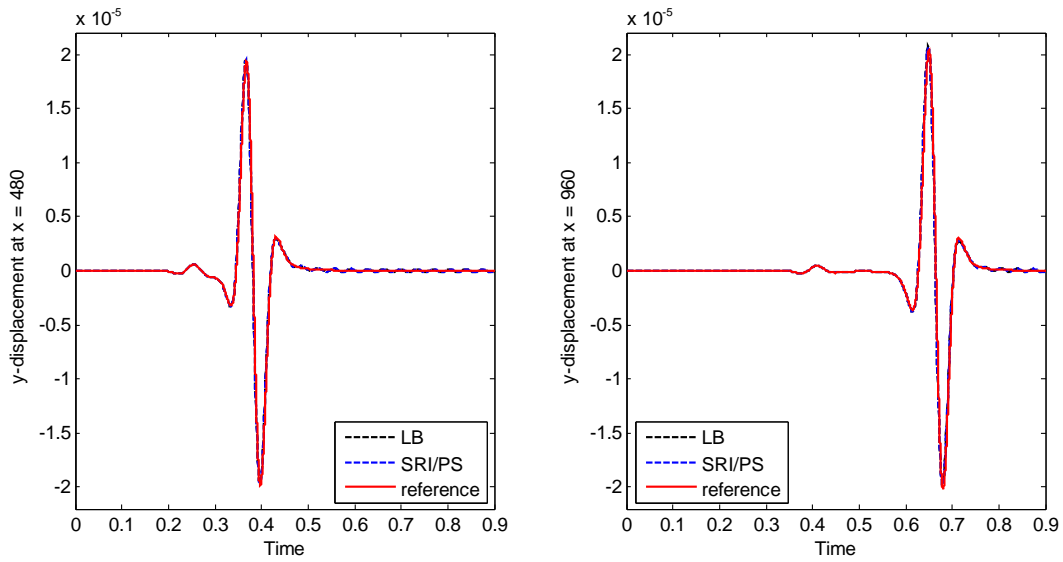
(b) $n = 3$
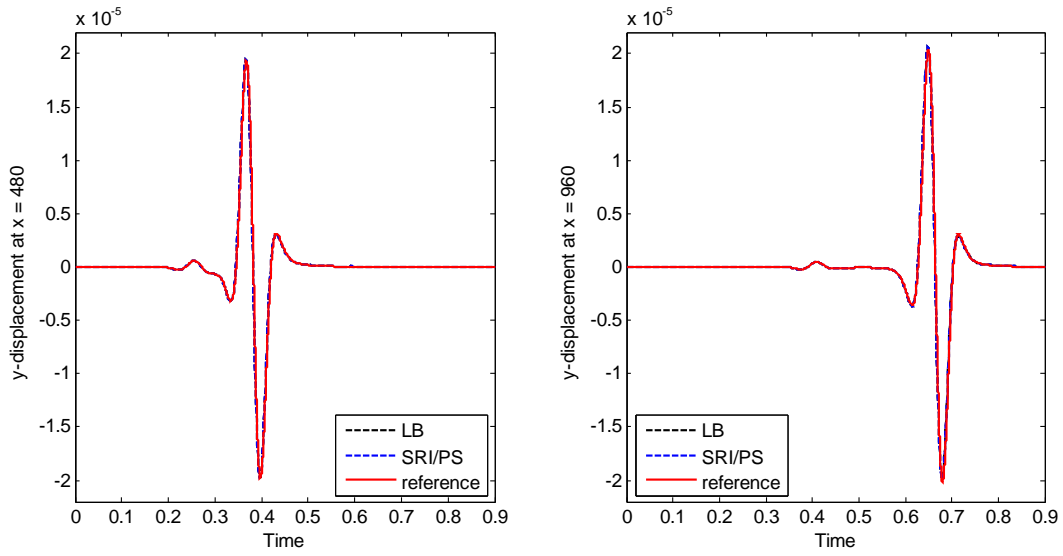
(c) $n = 4$

Figure 14. Time history of y-displacement at the receiver stations when $\upsilon = 0.25$ and $289{\times}289$ nodes are employed.
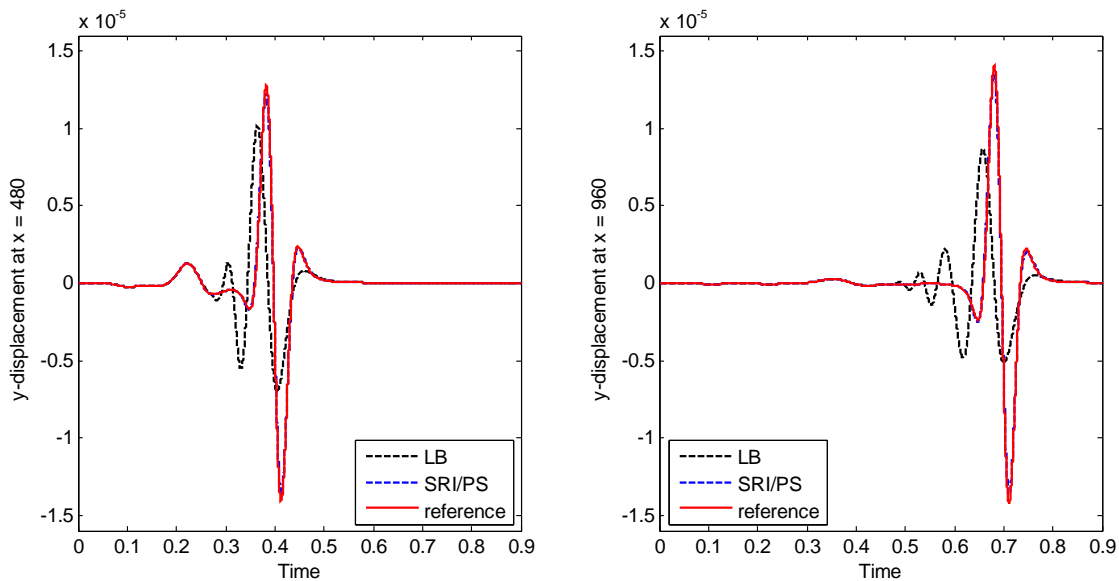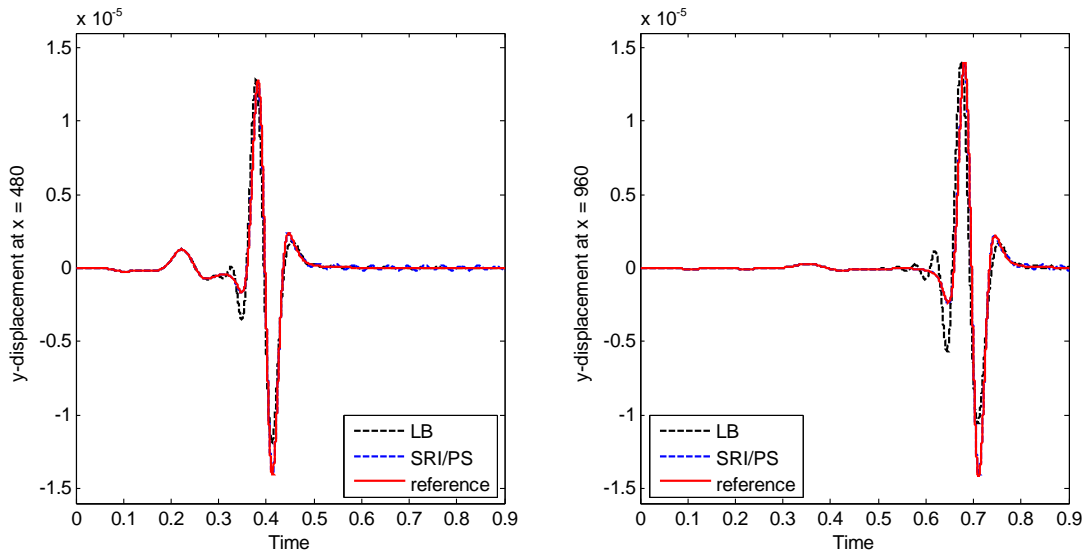

Figure 15. The reference solutions for (a) deviatoric and (b) dilatational energy densities at $t = 0.8$ when $\upsilon = 0.25$.

When the Poisson's ratio equals 0.4999, V_P (= 119.3×10^3) is two magnitude higher than V_S (= 1687) and V_R (= 1610), see (49). At frequency $2.5f_0$, the numbers of nodes per wavelength for the P-, S- and R-waves are ≈ 382, ≈ 5.4 and ≈ 5.2, respectively. For all elements, the time step increment is taken to be 24×10^{-6} which is again approximately 70% of the estimated critical time step increment of the fourth order elements, see Table 2. Figure 16 show the time histories of the y-displacement predicted by elements with order $n = 2$, 3 and 4 at the positions of the two receivers. The reference solution is obtained by the 288×288 fourth order elements and time step increment 2.4×10^{-6}. LB produces the most erroneous predictions which, however, improve with the element order. Predictions of the other elements are close to the reference solutions. Figure 17 portrays the reference solutions for the (a) deviatoric and (b) dilatational energy density distributions at $t = 0.8$. Unlike the case of $\upsilon = 0.25$, V_S and V_R differs by only 0.5%. That probably explains why the S-waves below the R-waves are connected in Figure 17(a) but not in Figure 15(a). In Figure 17(b), high intensity of dilatational energy can be noted in the R-waves at the free surface and at the lower end of the line of symmetry. The colour fringes in the lower half of the domain are dynamic and present the P-waves. Figures 18(a) and 18(b) show the deviatoric and dilatational energy density distributions predicted by the second order LB at $t = 0.8$, respectively. Ahead of the S-waves in Figure 17(a) is a cluster of vertical fringes which, however, cannot be seen in the reference solution in Figure 17(a). In the position occupied by the S-waves in Figure 18(b), the predicted dilatational energy density by the second order LB is less smooth compared with the reference solution in Figure 17(b). Furthermore, a small high energy intensity patch can be seen in the middle of the lower edge in Figure 18(b). Such a patch does not appear in the reference solution in Figure 17(b). Figures 18(c) and 18(d) show the predictions of the second order PS. They as well as the predictions by other high order elements are essentially the same as the reference solutions.
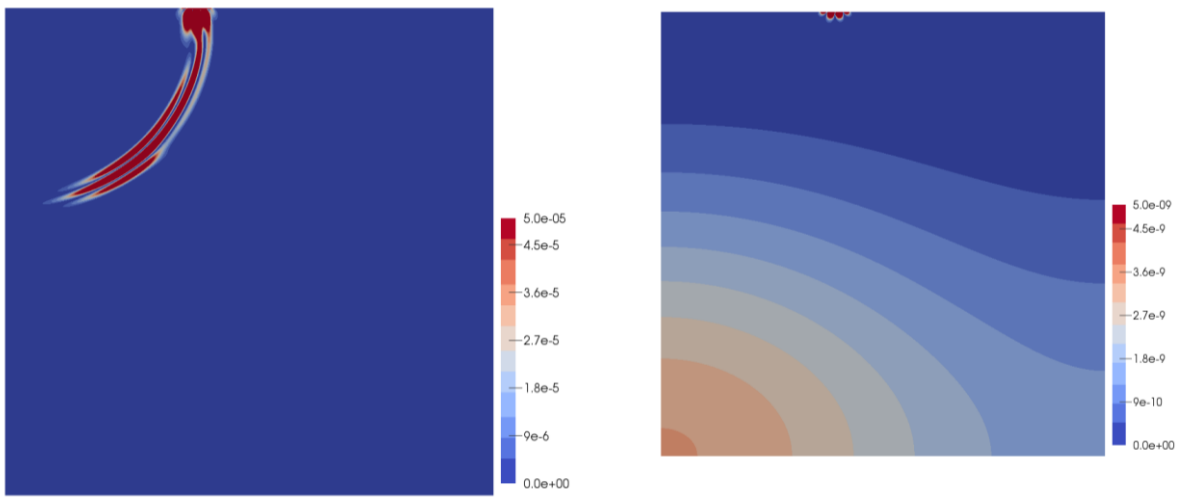

(a) $n = 2$

(b) *n* = 3
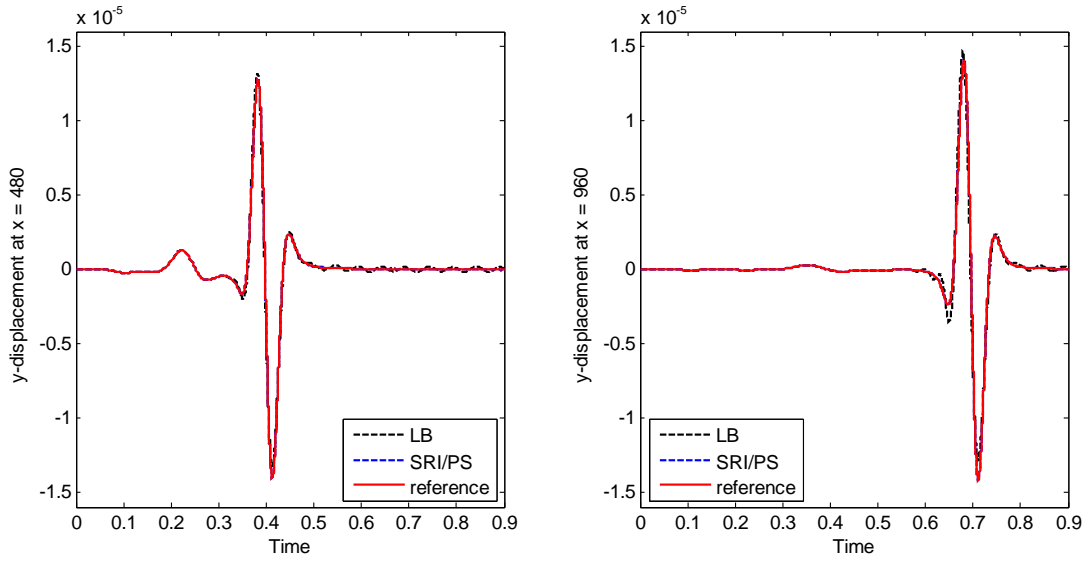
(c) *n* = 4

Figure 16. Time history of *y*-displacement at the two receiver stations when $\upsilon = 0.4999$ and 289×289 nodes are employed.

(a)

(b)

Figure 17. The reference solutions for (a) deviatoric and (b) dilatational energy densities at $t = 0.8$ when $\upsilon = 0.4999$.
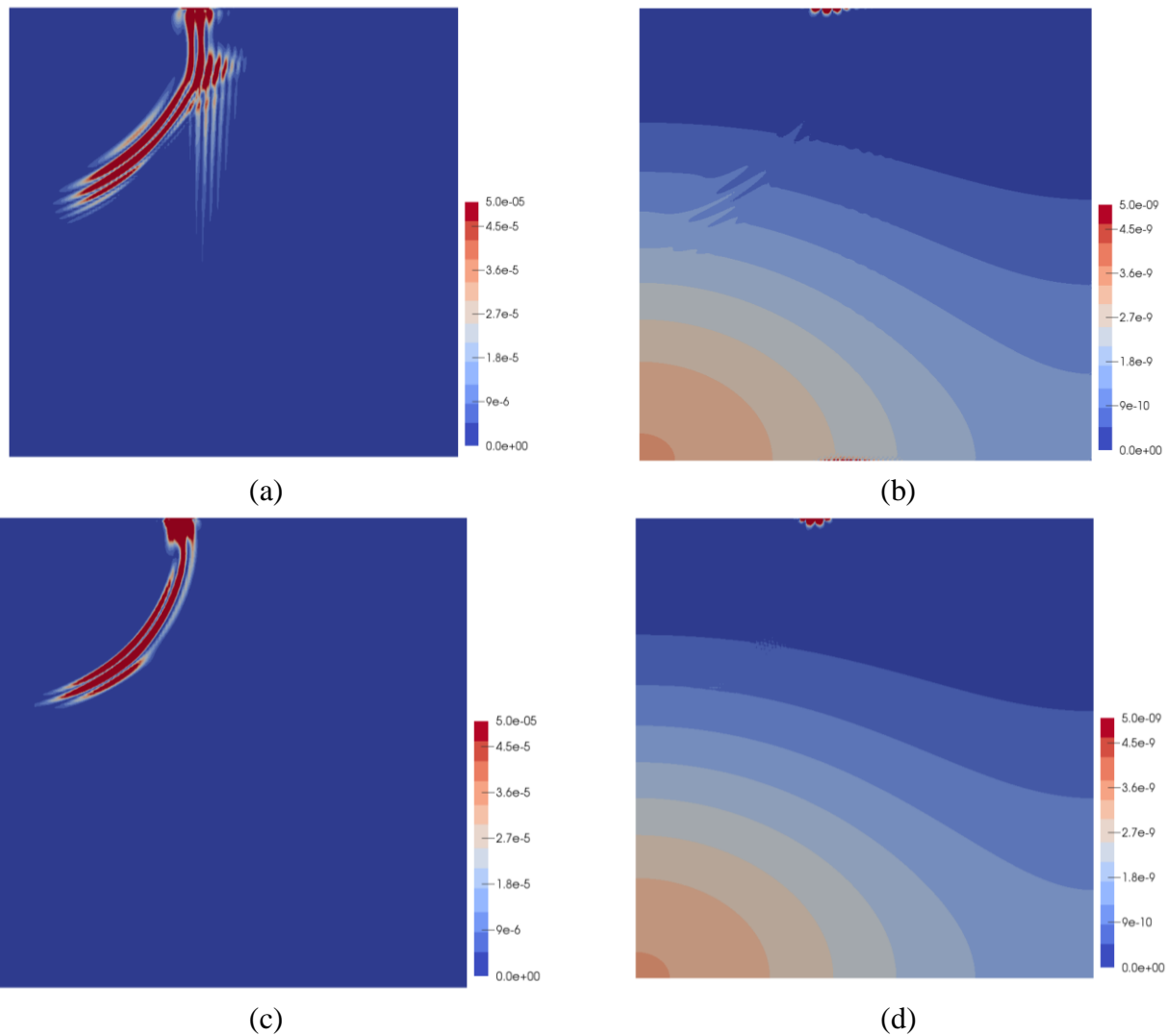
Figure 18. (a) Deviatoric and (b) dilatational energy densities predicted by second order LB; (c) deviatoric and (d) dilatational energy densities predicted by second order PS; $t = 0.8$, $v = 0.4999$ and 289×289 nodes are employed.

7.8 Wave Propagation Problem modelled by 217×217 Nodes

In the last subsection, only the second and third order LB do not produce predictions close to the reference solutions. Here, the same problem is re-analyzed using 217×217 nodes, i.e. the average nodal spacing increases from 10 to 40/3 which is excessively large for the second order elements.

For Poisson's ratio equal to 0.25, Figure 19 shows the time histories of the y-displacement predicted by third and fourth order elements at the positions of the two receivers. All elements yield predictions close to the reference solution but there are a bit of oscillations in predictions of the third order elements after the R-waves leave. The deviatoric and dilatational energy densities predicted by the third and fourth elements are graphically indistinguishable from the reference solutions in Figure 15.
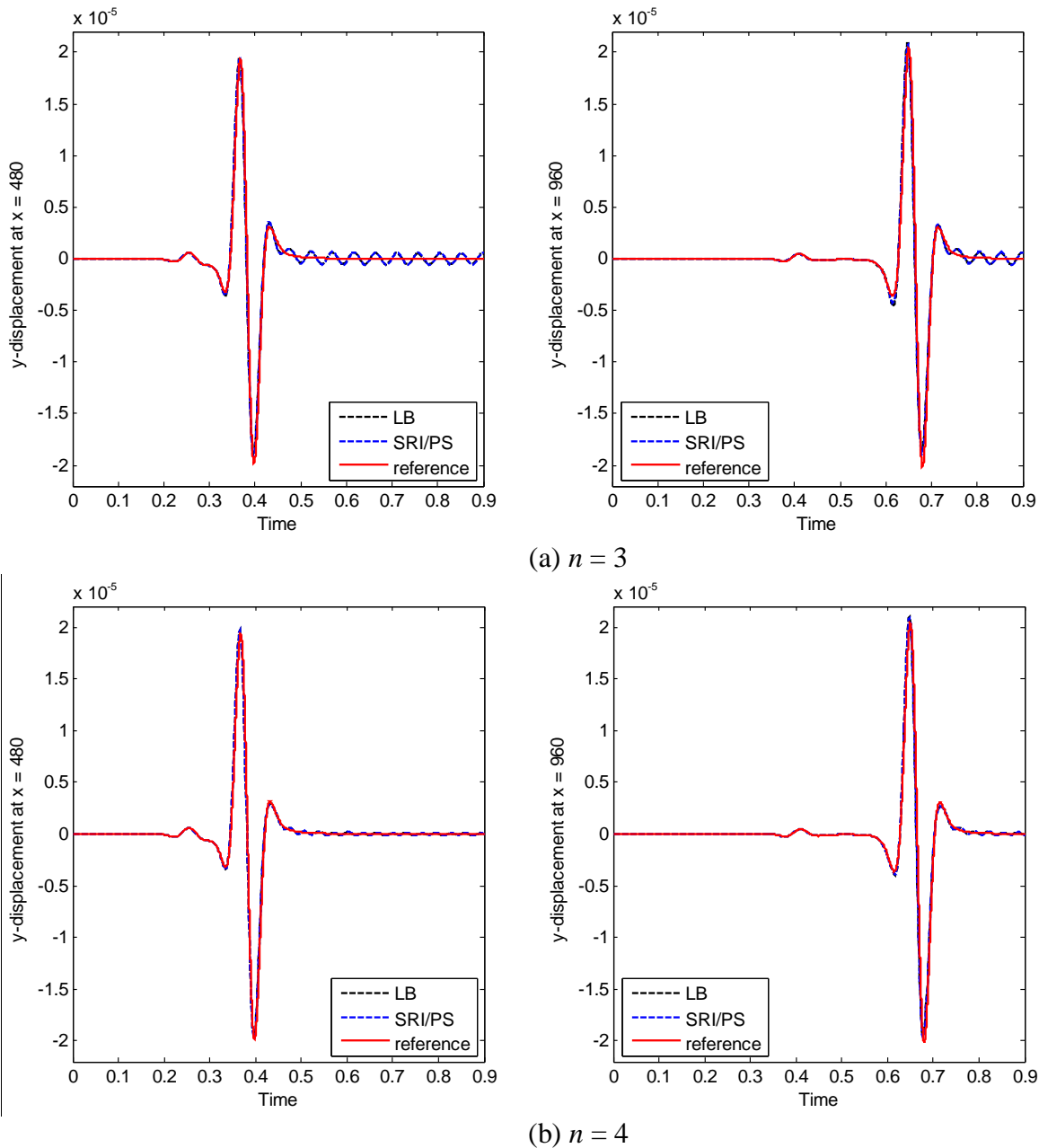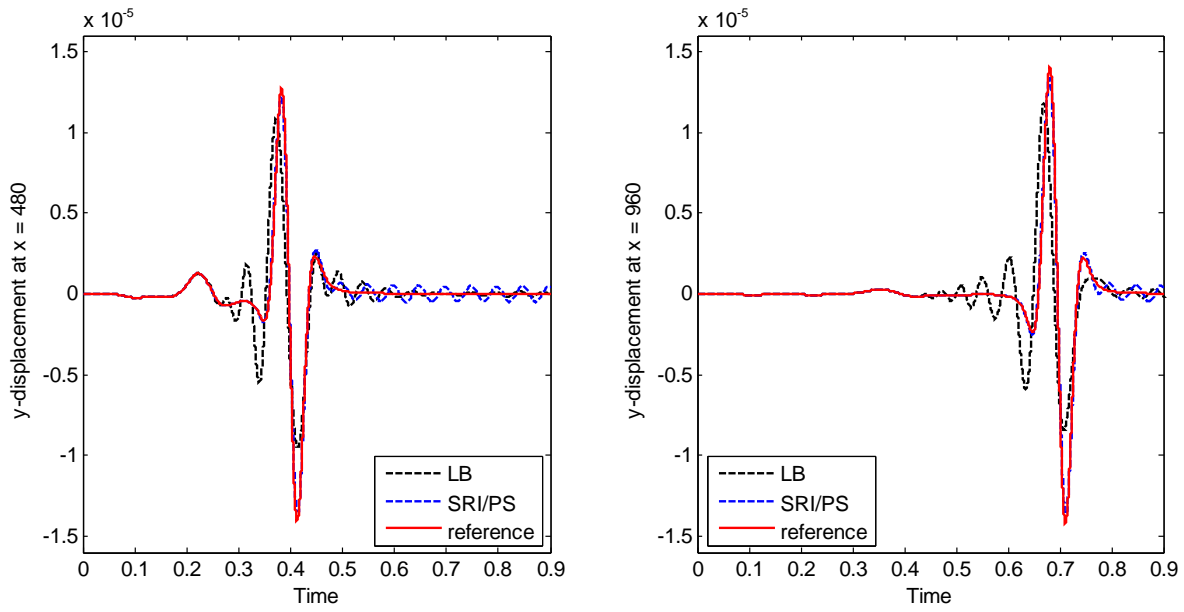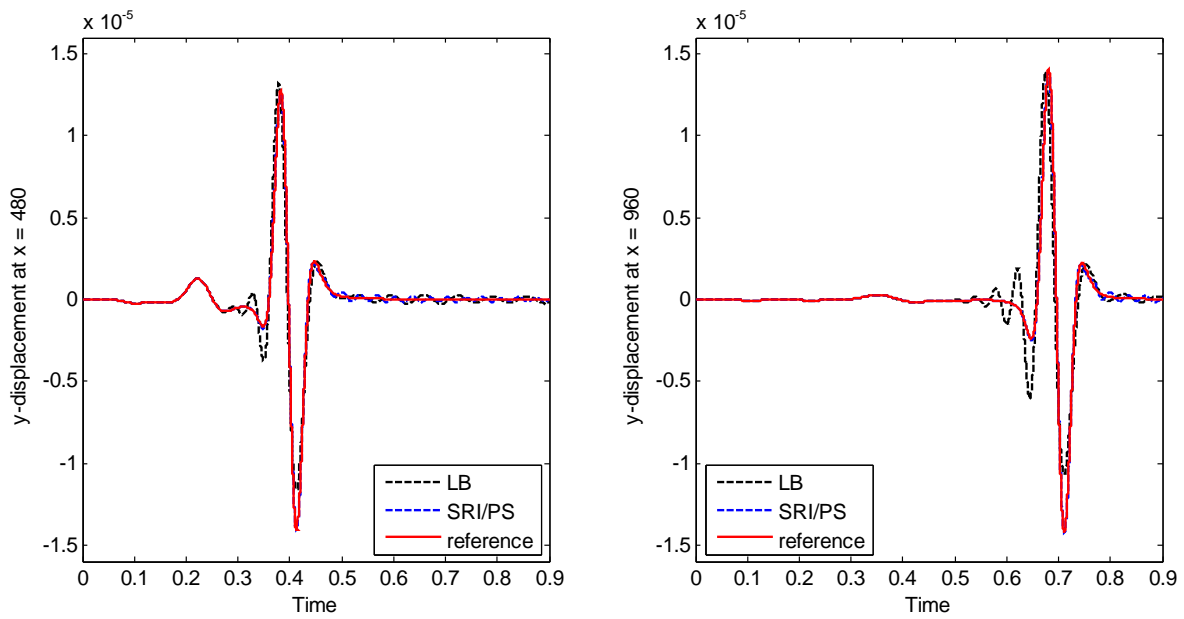
(a) $n = 3$

(b) $n = 4$

Figure 19. Time history of y-displacement at the receiver stations when $\upsilon = 0.25$ and 217×217 nodes are employed.

For Poisson's ratio equal to 0.4999, Figure 20 shows the time histories of the y-displacement predicted by third and fourth order elements at the positions of the two receivers. Both the third and fourth order LB elements oscillate considerably before the R-waves arrive whilst all elements oscillates but at much lower amplitudes after the R-waves leave. Figures 21(a) and 21(b) show the deviatoric and dilatational energy density distributions predicted by the third order LB at $t = 0.8$. Their differences with respect to the reference solution are similar to those yielded by the second order LB as shown in Figure 18(a) and Figure 18(b). In other words, there is a cluster of vertical fringes ahead of the S-wave in the deviatoric energy. Figures 21(c) and 21(d) show the energy distributions predicted by the third order PS. It can be seen that the vertical fringes ahead of the S-waves in the deviatoric energy and the dilatational energy is smoother than that of the third order

LB. The energy distributions of the third order PS and all fourth order elements are graphically indistinguishable from the reference solution.

(a) $n = 3$

(b) $n = 4$

Figure 20. Time history of y-displacement at the receiver stations when $\upsilon = 0.4999$ and 217×217 nodes are employed.

(a)   (b)

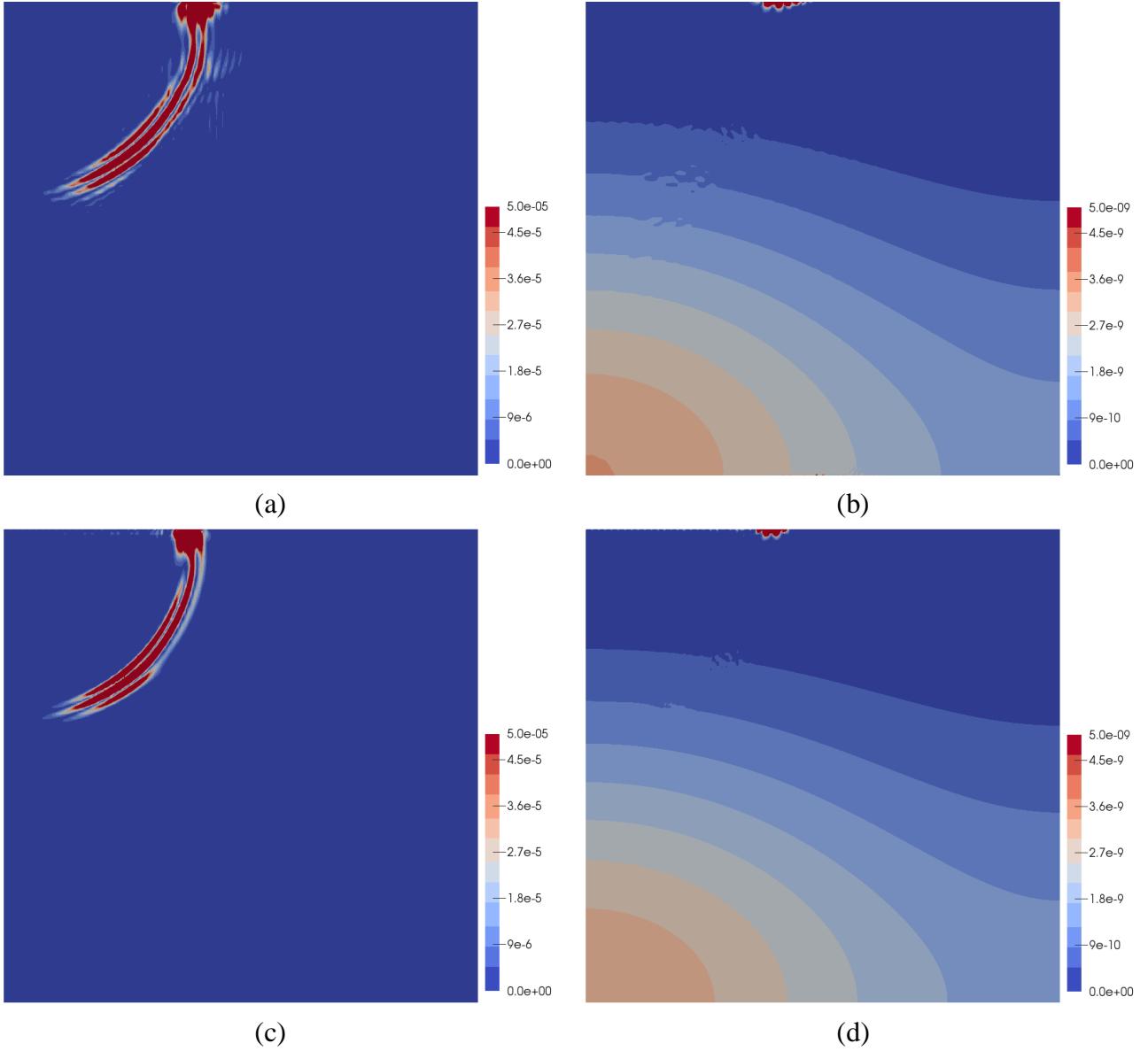(c)   (d)

Figure 21. (a) Deviatoric and (b) dilatational energy densities predicted by third order LB; (c) deviatoric and (d) dilatational energy densities predicted by third order PS; $t = 0.8$, $\upsilon = 0.4999$ and 217×217 nodes are employed.

7.9 Spherical Container under Internal Pressure

A spherical container with inner radius R_i ($= 5$) and outer radius R_o ($= 20$) under internal pressure P is considered [19, 20], see Figure 22. The exact displacement and stress solutions are

$$
\underline{u}^{exact} = \begin{Bmatrix} u_r^{exact} \\ u_z^{exact} \end{Bmatrix} = A \left(\frac{1}{3\lambda + 2\mu} + \frac{1}{4\mu} \frac{R_o^3}{R^3} \right) \begin{Bmatrix} r \\ z \end{Bmatrix}
$$

and

$$
\begin{Bmatrix} \sigma_r^{exact} \\ \sigma_z^{exact} \\ \sigma_\theta^{exact} \end{Bmatrix} = A\left(1 + \frac{1}{2}\frac{R_o^3}{R^3}\right) \begin{Bmatrix} 1 \\ 1 \\ 1 \end{Bmatrix} - \frac{3A}{2}\frac{R_o^3}{R^5} \begin{Bmatrix} r^2 \\ z^2 \\ 0 \end{Bmatrix} \quad , \quad \sigma_{rz}^{exact} = -\frac{3A}{2}\frac{R_o^3 rz}{R^5}
$$

where $A = PR_i^3 / (R_o^3 - R_i^3)$; λ and μ are Lame constants. This problem is analyzed by axisymmetric elements. The displacement and energy error plots are shown in Figure 23. The meshes with $m \times m$ elements where $m = 1, 2, 4$ and 8 are adopted for the h-convergence plots in Figures 23(a) to 23 (c). In the p-convergence plots in Figure 23(d), the 2×2 element mesh is employed. The stabilized elements are consistently more accurate than the conventional Lobatto elements for both $\upsilon = 0.25$ and 0.4999. Similar to the thick cylinder problem in Section 7.2, the accuracy differ by several orders of magnitude in some cases.
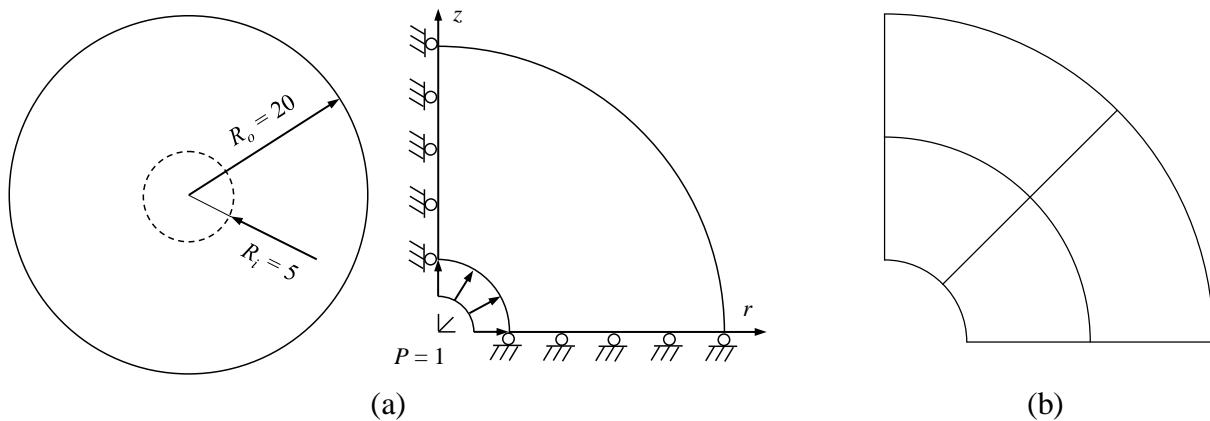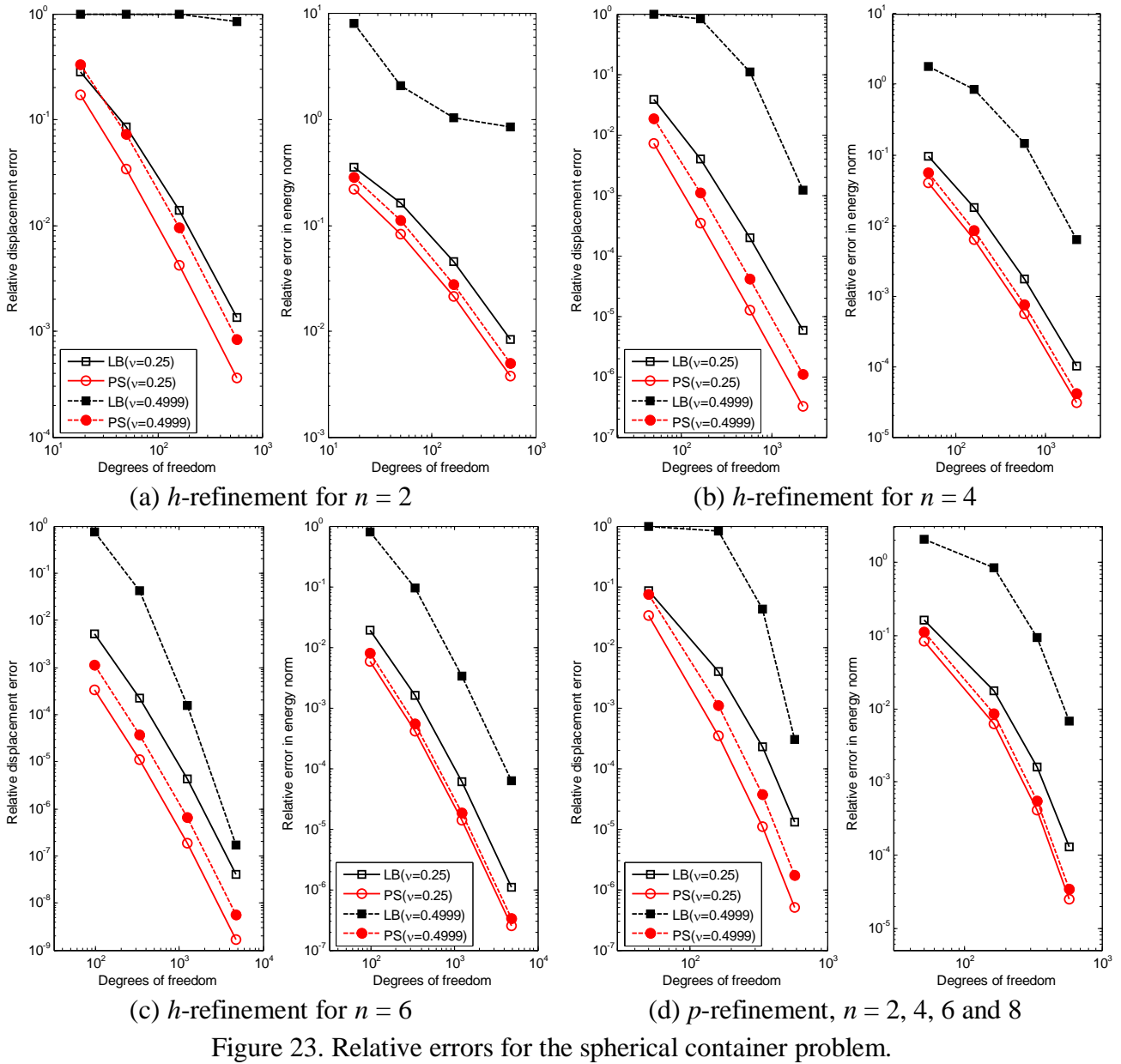

Figure 22. (a) The spherical container under internal pressure. (b) The 2×2 mesh of the axisymmetric elements.

8. CLOSURE

Stabilization vectors are devised for second and higher order uniformly reduced integrated (URI) Lagrange elements of which Lobatto elements commonly used in explicit dynamic analysis is a subset. Partially and fully stabilized elements are formulated by devising two and three stabilization vectors, respectively. They are computationally more efficient than the selectively reduced integration (SRI) element. From the numerical examples, partially and fully stabilized elements produce almost identical results. Their displacement predictions are always more accurate than the conventional Lobatto elements. When the material is far from incompressible, the stabilized elements and the conventional Lobatto elements yield similar errors in energy norm. When the material is nearly incompressible, the stabilized elements are also markedly more accurate in energy norm. In the wave dynamic example, the stabilized elements are also more accurate than the conventional Lobatto elements for nearly incompressible media. This advantage is of practical importance for wave analyses in bio-tissues and hydrated soils. The stabilized, SRI and conventional Lobatto elements exhibit spurious pressure oscillations in the renowned non-leaky

cavity problem. The oscillation in the stabilized and SRI elements can be eliminated by a simple technique which marginally reduces the rank of their penalty matrix arising from the dilatational energy.

(a) *h*-refinement for *n* = 2

(b) *h*-refinement for *n* = 4

(c) *h*-refinement for *n* = 6

(d) *p*-refinement, *n* = 2, 4, 6 and 8

Figure 23. Relative errors for the spherical container problem.

REFERENCE

[1] Patera AT, A spectral element method for fluid dynamics: Laminar flow in a channel expansion, Journal of Computational Physics, 54 1984 468-488.

[2] Maday Y, Meiron D, Patera AT, Rønquist EM, Analysis of iterative methods for the steady and unsteady Stokes problem: Application to spectral element discretizations, SIAM Journal on Scientific Computing, 14 1993 310-337.

[3] Komatitsch D, Vilotte JP, The spectral element method: An efficient tool to simulate the seismic response of 2D and 3D geological structures, Bulletin of the Seismological Society of America, 88 1998 368-392.

[4] Komatitsch D, Vilotte JP, Vai R, Castillo-Covarrubias JM, Sanchez-Sesma FJ, The spectral element method for elastic wave equations-application to 2-D and 3-D seismic problems, International Journal for numerical methods in engineering, 45 1999 1139-1164.

[5] Dauksher W, Emery AF, The solution of elastostatic and elastodynamic problems with Chebyshev spectral finite elements, Computer methods in applied mechanics and engineering, 188 2000 217-233.

[6] Canuto C, Hussaini MY, Quarteroni A, Zang TA, Spectral Methods: Fundamentals in Single Domains: Springer-Verlag, Berlin, 2006.

[7] De Basabe JD, Sen MK, Grid dispersion and stability criteria of some common finite-element methods for acoustic and elastic wave equations, Geophysics, 72 2007 T81-T95.

[8] Kudela P, Żak A, Krawczuk M, Ostachowicz W, Modelling of wave propagation in composite plates using the time domain spectral element method, Journal of Sound and Vibration, 302 2007 728-745.

[9] Seriani G, Oliveira SP, Dispersion analysis of spectral element methods for elastic wave propagation, Wave Motion, 45 2008 729-744.

[10] Witkowski W, Rucka M, Chróścielewski J, Wilde K, On some properties of 2D spectral finite elements in problems of wave propagation, Finite Elements in Analysis and Design, 55 2012 31-41.

[11] Xing Y, Liu B, High-accuracy differential quadrature finite element method and its application to free vibrations of thin plate with curvilinear domain, International journal for numerical methods in engineering, 80 2009 1718-1742.

[12] Zhong H, Yu T, A weak form quadrature element method for plane elasticity problems, Applied Mathematical Modelling, 33 2009 3801-3814.

[13] Pian THH, Derivation of element stiffness matrices by assumed stress distributions, AIAA Journal, 2 1964 1333-1336.

[14] Lee SW, Rhiu JJ, A new efficient approach to the formulation of mixed finite element models for structural analysis, International journal for numerical methods in engineering, 23 1986 1629-1641.

[15] Rhiu JJ, Lee SW, Russell RM, Two higher-order shell finite elements with stabilization matrix, AIAA journal, 28 1990 1517-1524.

[16] Sze KY, A novel approach for devising higher-order hybrid elements, International Journal for Numerical Methods in Engineering, 36 1993 3303-3316.

[17] Sze KY, Stabilization schemes for 12-node to 21-node brick elements based on orthogonal and consistently assumed stress modes, Computer Methods in Applied Mechanics and Engineering, 119 1994 325-340.

[18] Sze KY, Yi S, Tay MH, An explicit hybrid stabilized eighteen-node solid element for thin shell analysis, International journal for numerical methods in engineering, 40 1997 1839-1856.

[19] Sze KY, Wu D, Transition finite element families for adaptive analysis of axisymmetric elasticity problems, Finite Elements in Analysis and Design, 47 2011 360-372.

[20] Jog CS, Annabattula R, The development of hybrid axisymmetric elements based on the Hellinger–Reissner variational principle, International journal for numerical methods in engineering, 65 2006 2279-2291.

[21] Malkus DS, Hughes TJR, Mixed finite element methods—reduced and selective integration techniques: a unification of concepts, Computer Methods in Applied Mechanics and Engineering, 15 1978 63-81.

[22] Brito KD, Sprague MA, Reissner–Mindlin Legendre spectral finite elements with mixed reduced quadrature, Finite Elements in Analysis and Design, 58 2012 74-83.

[23] Belytschko T, Ong JSJ, Liu WK, Kennedy JM, Hourglass control in linear and nonlinear problems, Computer Methods in Applied Mechanics and Engineering, 43 1984 251-276.

[24] Belytschko T, Bachrach WE, Efficient implementation of quadrilaterals with high coarse-mesh accuracy, Computer Methods in Applied Mechanics and Engineering, 54 1986 279-301.

[25] Sze KY, Fan H, Chow CL, Elimination of spurious pressure and kinematic modes in biquadratic nine-node plane element, International journal for numerical methods in engineering, 38 1995 3911-3932.

[26] Reese S, Wriggers P, A stabilization technique to avoid hourglassing in finite elasticity, International Journal for Numerical Methods in Engineering, 48 2000 79-109.

[27] Gruttmann F, Wagner W, A stabilized one-point integrated quadrilateral Reissner–Mindlin plate element, International Journal for Numerical Methods in Engineering, 61 2004 2273-2295.

[28] Sze KY, Zheng SJ, Lo SH, A stabilized eighteen-node solid element for hyperelastic analysis of shells, Finite Elements in Analysis and Design, 40 2004 319-340.

[29] Liu GH, Sze KY, Axisymmetric quadrilateral elements for large deformation hyperelastic analysis, International Journal of Mechanics and Materials in Design, 6 2010 197-207.

[30] Simo JC, Rifai MS, A class of mixed assumed strain methods and the method of incompatible modes, International Journal for Numerical Methods in Engineering, 29 1990 1595-1638.

[31] Korelc J, Wriggers P, Consistent gradient formulation for a stable enhanced strain method for large deformations, Engineering Computations, 13 1996 103-123.

[32] Glaser S, Armero F, On the formulation of enhanced strain finite elements in finite deformations, Engineering Computations, 14 1997 759-791.

[33] Kasper EP, Taylor RL, A mixed-enhanced strain method: Part I: Geometrically linear problems, Computers & Structures, 75 2000 237-250.

[34] Romero I, Bischoff M, Incompatible Bubbles: A non-conforming finite element formulation for linear elasticity, Computer methods in applied mechanics and engineering, 196 2007 1662-1672.

[35] Bert CW, Malik M, Differential quadrature method in computational mechanics: a review, Applied Mechanics Reviews, 49 1996 1-27.

[36] Hughes TJR, The Finite Element Method: Linear Static and Dynamic Finite Element Analysis: Dover Publications, 2000.

[37] Szabó BA, Babuška I, Finite element analysis: John Wiley & Sons, New York, 1991.

[38] Timoshenko S, Goodier JN, Theory of Elasticity: McGraw-Hill, New York, 1970.

[39] Sani RL, Gresho PM, Lee RL, Griffiths DF, The cause and cure (?) of the spurious pressures generated by certain FEM solutions of the incompressible Navier-Stokes equations: Part 1, International Journal for Numerical Methods in Fluids, 1 1981 17-43.

[40] Noh G, Bathe KJ, An explicit time integration scheme for the analysis of wave propagations, Computers & Structures, 129 2013 178-193.

[41] Achenbach JD, Wave Propagation in Elastic Solids: North-Holland, 1973.

Appendix: Assembling the Element Stiffness Matrices

In this appendix, the LB and URI element stiffness matrices formed by the assembling procedure is presented. By recalling the property $L_i(l_j) = \delta_{ij}$, the derivatives for any interpolated variable ϕ at (l_k, l_l) with respect to the parametric coordinates are

$$\phi,_\xi \big|_{(\xi=l_k, \eta=l_l)} = \sum_{i,j=1}^{n+1} L_i'(l_k) L_j(l_l) \phi_{ij} = \sum_{i=1}^{n+1} L_i'(l_k) \phi_{il} = [L_1'(l_k),...,L_n'(l_k)] \begin{Bmatrix} \phi_{1l} \\ \vdots \\ \phi_{nl} \end{Bmatrix} = [L_1'(l_k),...,L_n'(l_k)] \cdot \underline{\phi}_{Ql} ,$$

$$\phi,_\eta \big|_{(\xi=l_k, \eta=l_l)} = \sum_{i,j=1}^{n+1} L_i(l_k) L_j'(l_l) \phi_{ij} = \sum_{j=1}^{n+1} L_j'(l_l) \phi_{kj} = [L_1'(l_l),...,L_n'(l_l)] \begin{Bmatrix} \phi_{k1} \\ \vdots \\ \phi_{kn} \end{Bmatrix} = [L_1'(l_l),...,L_n'(l_l)] \cdot \underline{\phi}_{Pk}$$

in which $\underline{\phi}_{Pi}$ and $\underline{\phi}_{Qi}$ are respectively the vectors containing the nodal values of ϕ in the following Lobatto node sets:

$$Pi = \{(l_i, l_1), (l_i, l_2), ..., (l_i, l_n), (l_i, l_{n+1})\} \quad \text{for } i = 1,..,n+1;$$

$$Qi = \{(l_1, l_i), (l_2, l_i), ..., (l_n, l_i), (l_{n+1}, l_i)\} \quad \text{for } i = 1,..,n+1,$$

see Figure 2(b) for illustration. Moreover, $L_i'(l_j)$ can be pre-computed as in the spectral and differential quadrature methods, see [35] among others. Through the chain rule of differentiation

$$\frac{\partial}{\partial x} = \frac{1}{J}\left(\frac{\partial y}{\partial \eta}\frac{\partial}{\partial \xi} - \frac{\partial y}{\partial \xi}\frac{\partial}{\partial \eta}\right), \quad \frac{\partial}{\partial y} = \frac{1}{J}\left(-\frac{\partial x}{\partial \eta}\frac{\partial}{\partial \xi} + \frac{\partial x}{\partial \xi}\frac{\partial}{\partial \eta}\right)$$

where $J = (\partial x/\partial \xi)(\partial y/\partial \eta) - (\partial y/\partial \xi)(\partial x/\partial \eta)$ is the Jacobian determinant, the strain component at the Lobatto node (i,j) can be expressed as:

$$\underline{\varepsilon}_{ij} = \begin{Bmatrix} \varepsilon_x \\ \varepsilon_y \\ \gamma_{xy} \end{Bmatrix}\Bigg|_{(\xi=l_i, \eta=l_j)} = \begin{Bmatrix} u,_x \\ v,_y \\ u,_y + v,_x \end{Bmatrix}\Bigg|_{(\xi=l_i, \eta=l_j)} = \underline{\underline{B}}_{PiQj} \underline{d}_{PiQj}$$

where $\underline{\underline{B}}_{PiQj}$ is the strain-displacement matrix for node (i,j) with respect to $\underline{d}_{PiQj}$ which is vector containing the $2(2n+1)$ nodal displacement components in the node sets Pi and Qj. Using the LBQ rule in which the integration points are the Lobatto nodes, the strain energy in the element can be expressed as:

$$\frac{1}{2}\langle \underline{\varepsilon}^T \underline{\underline{C}} \underline{\varepsilon} \rangle_{LBQ}^e = \frac{1}{2}\sum_{i,j=1}^{n+1}(w_i w_j J_{ij} \underline{\varepsilon}_{ij}^T \underline{\underline{C}} \underline{\varepsilon}_{ij}) = \frac{1}{2}\sum_{i,j=1}^{n+1}(w_i w_j J_{ij} \underline{d}_{PiQj}^T \underline{\underline{B}}_{PiQj}^T \underline{\underline{C}} \underline{\underline{B}}_{PiQj} \underline{d}_{PiQj}) = \frac{1}{2}\underline{d}^T \underline{\underline{k}}_{LB} \underline{d}$$

where w_i is the weight factor for the Lobatto node l_i, $J_{ij} = J\big|_{(\xi=l_i, \eta=l_j)}$. As dim.($\underline{\underline{B}}_{PiQj}^T \underline{\underline{C}} \underline{\underline{B}}_{PiQj}$) = $2(2n+1) \times 2(2n+1)$ is smaller or much smaller than dim.($\underline{\underline{k}}_{LB}$) = $2(n+1)^2 \times 2(n+1)^2$, the process of

forming $\underline{k_{LB}}$ from $\underline{\underline{B_{PiQj}^T}}\underline{\underline{C}}\underline{\underline{B_{PiQj}}}$ can be speeded up by using matrix assembling which is similar to that used in forming the system matrix from the element matrices.

For the URI element, the derivatives for any variable ϕ at RGQ point (g_k,g_l) with respect to the parametric coordinates are

$$\phi,_{\xi}\big|_{\xi=g_k,\eta=g_l} = \sum_{i,j=1}^{n+1} L_i'(g_k)L_j(g_l)\phi_{ij} \ , \ \phi,_{\eta}\big|_{\xi=g_k,\eta=g_l} = \sum_{i,j=1}^{n+1} L_i(g_k)L_j'(g_l)\phi_{ij} \tag{50}$$

As

$$\phi\big|_{\xi=l_i,\eta=g_l} = \sum_{m,j=1}^{n+1} L_m(l_i)L_j(g_l)\phi_{ij} = \sum_{j=1}^{n+1} L_j(g_l)\phi_{ij} \quad \text{and}$$

$$\phi\big|_{\xi=g_k,\eta=l_j} = \sum_{i,m=1}^{n+1} L_i(g_k)L_m(l_j)\phi_{im} = \sum_{i=1}^{n+1} L_i(g_k)\phi_{ij} \ , \tag{51}$$

Eq. (50) can be expressed as

$$\phi,_{\xi}\big|_{\xi=g_k,\eta=g_l} = \sum_{i=1}^{n+1} L_i'(g_k)\phi\big|_{\xi=l_i,\eta=g_l} = [L_1'(g_k),...L_n'(g_k)]\begin{Bmatrix} \phi\big|_{\xi=l_1,\eta=g_l} \\ \vdots \\ \phi\big|_{\xi=l_n,\eta=g_l} \end{Bmatrix} = [L_1'(g_k),...L_n'(g_k)]\cdot\underline{\phi_{\widehat{Q}l}} \ ,$$

$$\phi,_{\eta}\big|_{\xi=g_k,\eta=g_l} = \sum_{j=1}^{n+1} L_j'(g_l)\phi\big|_{\xi=g_k,\eta=l_j} = [L_1'(g_l),...,L_n'(g_l)]\begin{Bmatrix} \phi\big|_{\xi=g_k,\eta=l_1} \\ \vdots \\ \phi\big|_{\xi=g_k,\eta=l_n} \end{Bmatrix} = [L_1'(g_l),...,L_n'(g_l)]\cdot\underline{\phi_{\widehat{P}k}}$$

It can be seen that $\widehat{P}i$ and $\widehat{Q}i$ are respectively the vectors containing the values of the following auxiliary node sets:

$$\widehat{P}i = \{(g_i,l_1),(g_i,l_2),...,(g_i,l_n),(g_i,l_{n+1})\} \quad \text{for } i = 1,..,n,$$

$$\widehat{Q}i = \{(l_1,g_i),(l_2,g_i),...,(l_n,g_i),(l_{n+1},g_i)\} \quad \text{for } i = 1,..,n.$$

see Figure 2(c) for illustration. Again, $L_i'(g_j)$ can be pre-computed. Similar to the standard Lobatto element, the strain components at each RGQ point and the strain energy of the element can be expressed as:

$$\underline{\widehat{\varepsilon}_{ij}} = \begin{Bmatrix} \varepsilon_x \\ \varepsilon_y \\ \gamma_{xy} \end{Bmatrix}\Bigg|_{(\xi=g_i,\eta=g_j)} = \begin{Bmatrix} u,_x \\ v,_y \\ u,_y + v,_x \end{Bmatrix}\Bigg|_{(\xi=g_i,\eta=g_j)} = \underline{\underline{\widehat{B}_{\widehat{P}i\widehat{Q}j}}}\,\underline{d_{\widehat{P}i\widehat{Q}j}} \ ,$$

$$\frac{1}{2}\langle\underline{\varepsilon}^T\underline{\underline{C}}\underline{\varepsilon}\rangle_{RGQ}^e = \frac{1}{2}\sum_{i,j=1}^{n}(\widehat{w}_i\widehat{w}_j\widehat{J}_{ij}\underline{\widehat{\varepsilon}_{ij}^T}\underline{\underline{C}}\underline{\widehat{\varepsilon}_{ij}}) = \frac{1}{2}\sum_{i=1}^{n}(\widehat{w}_i\widehat{w}_j\widehat{J}_{ij}\underline{d_{\widehat{P}i\widehat{Q}j}^T}\underline{\underline{\widehat{B}_{\widehat{P}i\widehat{Q}j}^T}}\underline{\underline{C}}\underline{\underline{\widehat{B}_{\widehat{P}i\widehat{Q}j}}}\underline{d_{\widehat{P}i\widehat{Q}j}}) = \frac{1}{2}\underline{\widehat{d}}^T\underline{\underline{\widehat{k}}}\underline{\widehat{d}} \tag{52}$$

where $\widehat{\underline{\underline{B}}}_{\hat{P}i\hat{Q}j}$ is the strain-displacement matrix for the RGQ point (g_i,g_j) with respect to $\underline{d}_{\hat{P}i\hat{Q}j}$ which is vector containing the $4(n+1)$ displacement components in the auxiliary node sets $\widehat{P}i$ and $\widehat{Q}j$, $\widehat{J}_{ij} = J\big|_{(\xi=g_i,\eta=g_j)}$ and $\widehat{\underline{d}}$ is vector containing the $4n(n+1)$ displacement components in the auxiliary node sets $\widehat{P}i$ and $\widehat{Q}i$ for $i = 1,..,n$. Again, $\widehat{\underline{\underline{k}}}$ can be assembled from $\widehat{\underline{\underline{B}}}^T_{\hat{P}i\hat{Q}j}\underline{\underline{C}}\,\widehat{\underline{\underline{B}}}_{\hat{P}i\hat{Q}j}$. To derive the element stiffness matrix, the relation between the nodes and auxiliary nodes can be expressed as:

$$\widehat{\underline{d}} = \underline{\underline{T}}_a\underline{d} \tag{53}$$

in which $\underline{\underline{T}}_a$ is a sparse transformation matrix with $n+1$ non-zero entries per row. From (52) and (53), the stiffness matrix of the URI element is

$$\underline{\underline{k}}_{URI} = \underline{\underline{T}}_a^{\,T}\,\widehat{\underline{\underline{k}}}\,\underline{\underline{T}}_a \tag{54}$$